NANO CUBESATS FOR DARK AGES EXLORATION

_____

A Thesis

presented to

the Faculty of Natural and Applied Sciences

at Notre Dame University-Louaize

_____

In Partial Fulfillment

of the Requirements for the Degree

Master of Science

In Astrophysics
_____

by

MARWAN MALKOUN

SEPTEMBER 2020

Notre Dame University - Louaize

Faculty of Natural and Applied Sciences

Department of Physics and Astronomy

We hereby approve the thesis of

Marwan Malkoun

Candidate for the degree of Master in Astrophysics

_____

Dr. Bassem Sabra   Supervisor, Chair

_____

Dr. Marwan Gebran   Committee Member

_____

Dr. Wehbeh Farah   Committee Member

ACKNOWLEDGEMENTS

TABLE OF CONTENTS

LIST OF ILLUSTRATIONS

LIST OF TABLES

ABSTRACT

The Dark Ages, a period stretching from 400 thousand years to 400 million years after the big bang, is the least known era in the evolution of our universe, as no visible light was emitted. However, another type of radiation was available, the Hydrogen 21cm. It reaches us at frequencies between 1.5 and 30MHz. The ideal way to detect it, involves antennas placed in a fixed orbit around the dark side of the moon where it is shielded from electromagnetic interference emitted from earth.

Keywords: Dark Ages, Hydrogen 21 cm, CubeSats, Lunar orbit.

L'âge sombres, une période s'étendant de l'ans 400 mille jusquà 400 millions d'années après le big bang, est l'ère la moins connue de l'évolution de notre univers, car aucune lumière visible n'a été émise. Cependant, un autre type de rayonnement était disponible, l'hydrogène 21cm. Il nous parvient à des fréquences comprises entre 1,5 et 30 MHz. Le moyen idéal pour le détecter implique des antennes placées sur une orbite fixe autour du côté sombre de la lune où elle est protégée des interférences électromagnétiques émises par la terre.

Mots-clés: Âges sombres, Hydrogène 21 cm, CubeSats, orbite lunaire.

Chapter 1

INTRODUCTION

Astronomy's only medium to observe and study the universe is through the light that we receive on Earth. By studying and dissecting this light we can learn a great deal of things like the composition of stars, their formation, and the evolution of our universe. This light is what composes the whole electromagnetic spectrum which spans from gamma rays, having the highest frequencies and the shortest wavelengths, to radio waves which have the smallest frequencies, and thus the largest wavelengths. One of the ranges that the visible objects in the sky fall into is between 380 nm to 700 nm of the electromagnetic spectrum. The latter is the only range that the human eye is sensitive to. These visible objects are observed through optical telescopes, positioned either in specific remote locations on Earth, such as the Very Large Telescope in the Atacama Desert of northern Chile mounted at an altitude of 2,635m, or in orbit such as the Hubble Space Telescope. As Earth's atmosphere works as a filter blocking most of the electromagnetic radiation, only visible light and some UV and infrared radiation pass through. Astronomical objects such as stars, galaxies, clusters, and nebulae, emit light in all the ranges of the electromagnetic spectrum; Gamma rays, X-rays, UV, infrared, microwave, and radio waves. As such, in order to detect these objects in all of their ranges, other instruments are needed such as radio and gamma telescopes, ideally placed in orbit above Earth's atmosphere, to assure the best reception quality.

One of today's most sought after scientific topics that still holds many unknowns is the Dark Ages. This period, which stretched from 400 thousand years to 400 million years after the Big Bang, didn't experience any emission of visible light, and as such is the least known era in the evolution of our universe. However, another type of emission was available, which manifested in the form of neutral hydrogen 21 cm transition lines.

1.1 The Big Bang

To have a better grasp on the importance of this era, it is preferable to know some background. After years of observations and experiments, the best theory adopted to describe the beginning and formation of the universe is the Big Bang Theory. It postulates that it all started 13.75 billion years ago with a huge explosion, transforming an infinitesimally small universe into an exponentially expanding one, and while doing so, passing through critical periods. In the first 10 seconds of its creation, the universe has witnessed a cosmic inflation, the separation of the primordial force into the four forces that we know today (electromagnetism, weak and strong nuclear forces, and gravity), and the formation of elementary particles described in the standard model.

The immense amount of energy introduced into this incredibly small space-time that was the universe, caused it to increase its size by a factor of 10^{30}. Some residual vacuum energy remained after the inflation, which accelerated the rate of expansion while gravity pushed in the opposite direction. This energy, whose origins remains unknown, is called dark energy.

Elementary Particles

The standard model includes 61 elementary particles: three generations of matter particles, each consisting of two leptons and two flavors of quarks which each come in three different colors (24 in total), the anti-particles of all these (48 in total), 12 force particles: a photon, W^+, W^-, and Z^0 particles and eight gluons and a Higgs boson (figure 1.1).

A mysterious and unknown particle should be added to the above-mentioned ones. The study of large structures and the motion of galaxies and clusters of galaxies has led to the conclusion that another type of invisible matter exists and is so far undetectable. In a brilliant effort of imagination, this mysterious particle was called dark matter. Dark matter is believed to consist mostly of WIMPs (weakly interacting massive particles), an unknown matter, similar to neutrinos but much more massive. A smaller and less verified portion of dark matter is made up of massive astrophysical compact halo objects (MACHOs), which emit little or no radiation.

The interaction of all of these particles make up the universe that we know. As the universe cools down, energies are no longer sufficient to break the bonds between
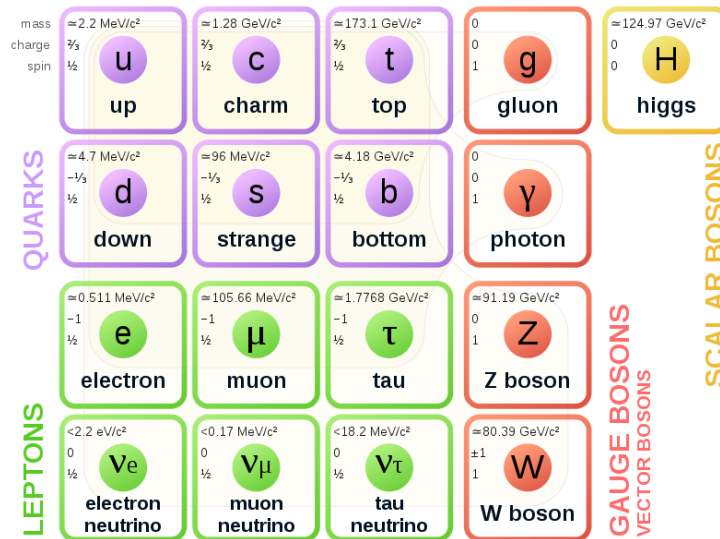
Figure 1.1: The Particles in the Standard Model: The six quarks (violet) and six leptons (green) are organized in three families; the four gauge bosons are shown in red. The numbers in each box indicate particle mass, charge (in units of the elementary charge) and spin. All particles have an antiparticle, except the photon and the Z-boson, which are their own antiparticles. Source: Wikipedia

quarks (the smallest constituents of matter). As such hadrons start to form, like protons and neutrons (made up of combinations of three quarks); And as temperatures continue to drop, hadrons and anti-hadrons pairs, followed by leptons and anti-leptons pairs start to annihilate each other respectively.

At 100 seconds, temperatures are around 10^9 kelvin, enough for primordial nucleosynthesis to take place. In other words, protons and neutrons can now bind together and remain in that state long enough for further reactions to take place (figure 1.2). After the proton picks up a neutron, it becomes a heavier isotope of hydrogen known as deuterium; As such, chain reactions will continue, forming new heavier elements (helium, lithium, beryllium, etc.). By the end of nucleosynthesis, ^{4}He, the most stable isotope of helium will account for 24% of the total mass of visible matter, and the remaining 76% are unreacted hydrogen (^{1}H). These nuclear reactions transform the charged plasma, initially composed of protons, neutrons, electrons and photons to one with positively charged hydrogen and helium, electrons and photons.

By the end of the first 100 seconds, the universe is dominated by dark energy, contributing to the majority of the mass-energy in it (68.3%), followed by a large portion of dark matter (26.8%), and a small amount of visible matter (4.9%), consisting mainly of hadrons (protons and neutrons), leptons (mostly electrons), and photons.

Before continuing with the journey of evolution, it is important to highlight some of the quantum properties of the elementary particles.
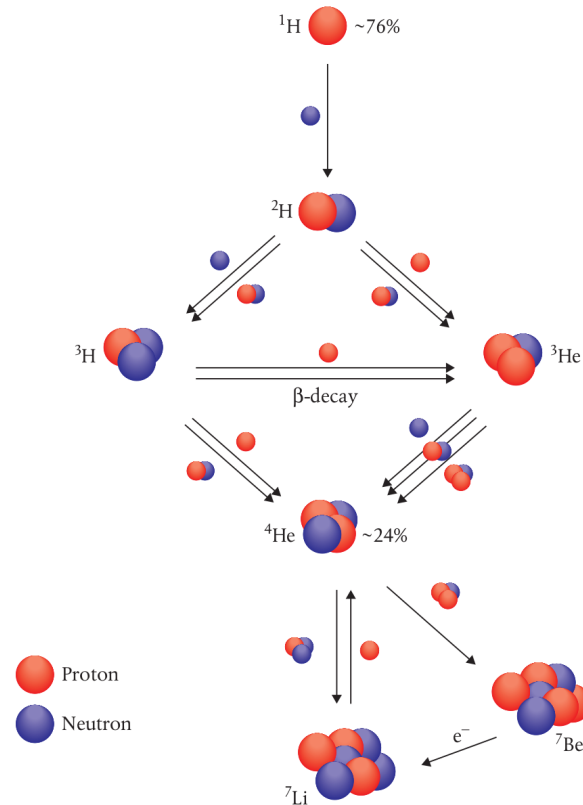
Figure 1.2: Sixteen of the most important nuclear reactions involved in primordial nucleo- synthesis. These are shown schematically in terms of the reactions of protons (red balls) and neutrons (blue balls). For simplicity, not all the products of the reactions are shown. Source: Origins

1.2 The Quantum World

In the 1920s, scientists discovered that the elementary particles behave differently under different circumstances. At times, they behave like chunks of particles, and at other times, they behave like waves much as ripples of water in a pond. The phenomenon is known as the wave-particle duality and is the basis of quantum theory. The best demonstration of this is the famous beam of electrons through two narrow slits experiment, where the resulting interference pattern seen on the screen proves the duality nature of the electron (figure 1.3). As such, there are two explanations for the repulsive forces acting on two colliding electrons. The wave approach is seen

through the manifestation of the electron's electromagnetic fields which themselves repel each other once they overlap. The particle approach states that the electrons exchange a photon once they reach a critical distance, and this exchanged photon carries momentum from one electron to the other, thus changing the momentum of both, resulting in a recoil. This is how the photon became the carrier of the electromagnetic force.
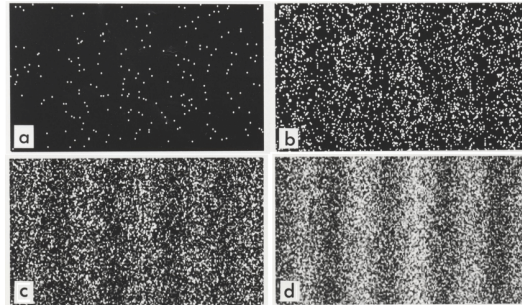
Figure 1.3: Results of a double-slit-experiment performed by Dr. Tanamura showing the build-up of an interference pattern of single electrons. Numbers of electrons are 200 (a), 6000 (b), 40000 (c), 140000 (d). Source: Researchgate

Spin

Another intrinsic property of the photon that should be emphasized is its spin or angular momentum. Although a misleading term, spin does not refer to self-rotation. Experiments have shown that a conservation of angular momentum is always maintained throughout interactions between matter and photons. This could be demonstrated with an intense beam of photons having aligned spins; this beam will exert a torque when directed towards a certain target, making it rotate.

Heisenberg's Uncertainty Principle

When measuring physical properties of wave-particle entities, such as position, one can superpose multiple waves having different wavelengths. This superposition will result in a spread of wavelengths having a peak in a specific location in space and small amplitudes everywhere else. It was discovered that the wavelength and momentum of a quantum-wave particle are inversely proportional. As such, one can measure the position of a quantum wave-particle but at the cost of uncertainty in its momentum.

The repercussions of this principle are quite profound. When measured, the energy of an electromagnetic field in a vacuum should be zero, and thus its rate of change should be zero. However, the uncertainty principle forbids such a result. As such, the vacuum experiences fluctuations of the electromagnetic field, which eventually averages to zero but, can be non-zero at individual points in space and time. Those fluctuations, imprinted on the large-scale structure of the universe by cosmic inflation, are responsible for part of the anisotropy in the universe.

1.3 The Dark Ages

From 100 seconds until 380,000 years, the universe experienced a period of relative calm. At around 380,000 years after the Big Bang, temperatures reached values around 3,000 kelvin; this marked the beginning of the Dark Ages. At these temperatures, it was possible for photons to separate from protons and electrons. This is known as the last scattering period, where light can freely travel and matter starts to take shape in the form that we know today. As such, recombination was initiated; free protons start to combine with free electrons to form neutral hydrogen atoms. The universe becomes transparent, flooded with the light released from recombination. This is the oldest light in the universe and it spans a broad range of wavelengths, peaking in the infrared. With the expansion of the universe, this light cools down and its wavelength stretches and reaches us from all directions uniformly. It can be detected on TV sets as white noise and is known as the cosmic microwave background (CMB) (figure 1.4).
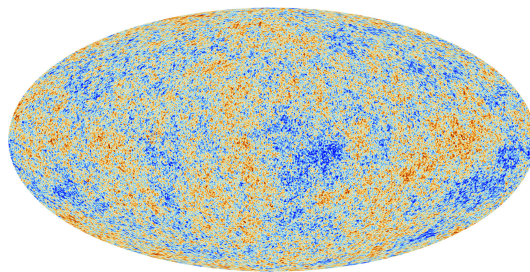
Figure 1.4: Detailed, all-sky map of temperature variations in the cosmic background radiation derived from data obtained from Planck. Red colors indicate higher temperatures and blue indicate cooler ones. Source: ESA

The previously mentioned neutral hydrogen atom is in its stable state when its electron and proton are spinning in opposite directions. While hydrogen atoms collide

with other free electrons and protons, in rare cases the spin of the electron will flip, making it rotate in the same direction as the proton. The electron will flip back to its original state after a couple of million years to go back to its natural state. While doing so, it will release a photon having a wavelength of 21 cm. Detecting and studying this specific wavelength of the CMB will give insights into the neutral hydrogen formation period, which is the dark ages.
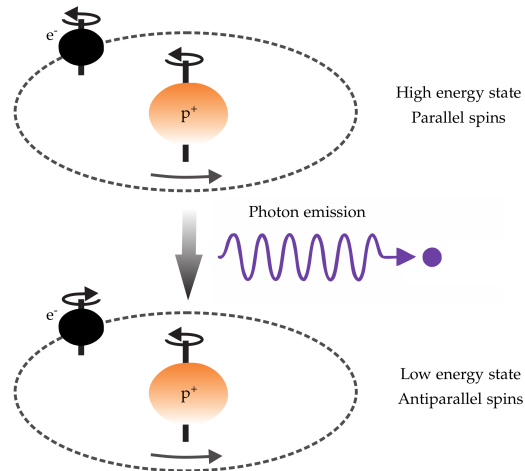
Figure 1.5: The hydrogen emission mechanism. Source: Alexandru, 2015

Anisotropies such as the ones previously mentioned, were detected in the CMB, which indicates that the universe contained inhomogeneities. Other evidence of these inhomogeneities are seen on the large scale in galaxy distribution, and in the existence of superclusters and voids. A quick description of the formation of these clusters and voids highlights the importance of studying the 21 cm radiation.

Due to small gravitational instabilities, certain regions in the universe will have either higher or lower densities. As such, higher density regions will slow the expansion rate and lower density regions will accelerate the expansion rate, creating small perturbations. Over time, gravity will drive these small perturbations to grow into large structures, which eventually collapses, forming sheets, filaments, voids and halos (figure 1.5). Moreover, excess dark matter will gather to form dark matter halos in high density regions (the slightly hotter regions in figure 1.4). Due to their gravity, these halos will evolve by pulling other halos together, and over time reaching enormous sizes. They will reach a certain point when their gravity is high enough to start influencing the baryonic matter trapped inside of them. This matter when condensed into a cloud that is cool enough, will collapse on itself and ignite a series of nuclear fusion reactions; the first stars are born.
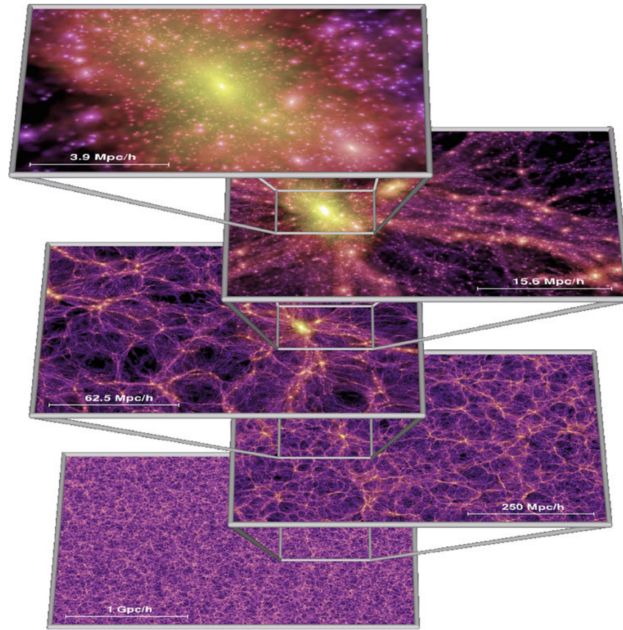
Figure 1.6: Distribution of matter in slices of thickness $15h^{-1}$ Mpc each, computed in the Millennium Simulation. Halos, sheets and filaments can be clearly distinguished on the three images in the middle. Source: Extragalactic Astronomy And Cosmos

1.4 The Mission

The spin flip transition of neutral hydrogen is used to map the hydrogen rich areas in our universe. The study of this radiation will help answer many fundamental questions in cosmology, such as the formation of the first stars, knowing the universe's fundamental parameters, and the initial conditions for the formation of primordial molecules. Other discoveries can be made as well, such as tracing the footprints of the early universe, mapping the interstellar medium, detecting exoplanets from planetary radio emission, and studying space weather and solar bursts. This wavelength, after traveling enormous distances through the universe, reaches us as a stretched microwave radiation, redshifted to low frequencies between 1.5 MHz and 30 MHz. These low frequencies are the least explored ranges of the electromagnetic spectrum, due to two obstacles. The first being our ionosphere, which acts as a shield, bouncing of frequencies below 10 MHz, and the second is the radio frequency interference emitted by earth-based instruments. These effects make it nearly impossible for earth-based observatories to detect such frequencies, thus creating a need for alternative solutions, such as space based radio telescopes.

This paper explores one of the aforementioned solutions: the development of a

mission for a Nano CubeSat in a fixed orbit around the dark side of the moon. This CubeSat will have as a payload, a short dipole antenna to detect the neutral hydrogen 21 cm transition lines. Nano CubeSats are the upcoming competitive solution for space exploration and present a great opportunity for this scientific space mission. The latter is due to their relatively cheap costs and small dimensions which makes them more efficient to build and manage. Since the lunar farside is always shielded from earth's radio frequency interference, plasma noise from solar winds, and auroral radiation, it makes it the ideal place to set Nano CubeSats and detect this range of low frequencies. The first part of this report looks at the hydrogen 21 cm transition line properties in order to figure out the best detection methods. The second part deals with the Nano CubeSat payload, which is the antenna required for those detections. The third part tackles the CubeSats, their architecture, and data retrieval and transmission. Finally the space mission outline, and orbit design around the moon are analyzed.

C h a p t e r   2

HYDROGEN 21 CM

Composing 75% of matter in the universe, hydrogen is an ideal candidate to study the intrinsic characteristics of the gas. This chapter will focus on the 21 cm transition line of neutral hydrogen, resulting from the hyperfine splitting of the 1S ground state. This split, which is caused by the magnetic moment interaction of the proton and electron, leads to two energy levels separated by 5.9×10^{-6} eV, corresponding to a wavelength of 21 cm and a frequency of 1420 MHz.

Predicted by Van de Hulst in 1942, the 21 cm line was first detected in 1951 by Ewen & Purcell. Existing radio telescopes are able to detect this line and use it to probe the velocity distribution of gas within galaxies. For cosmological research, the line is used as a probe of gas along the line of sight to some background radio source. The measured signal depends on the radiative transfer through the gas in the line of sight,

$$\frac{dI_\nu}{ds} = -\alpha_\nu I_\nu + j_\nu \tag{2.1}$$

Where I_ν is the specific intensity, and α_ν and j_ν describe the absorption and emission by the gas, respectively. This expression describes the energy carried by rays traveling along a given direction, per unit area, frequency, solid angle and time. Using the Rayleigh-Jeans formula $I_\nu = 2k_B T_b \nu^2/c^2$ to relate I_ν to a brightness temperature T_b, where c is the speed of light and k_B is Boltzman's constant, and using the definition of the optical depth $\tau = \int ds \alpha_\nu(s)$, equation (2.1) can be rewriten in terms of temperatures,

$$T_b^{obs} = T_{ex}(1 - e^{-\tau_\nu}) + T_R(\nu)e^{-\tau_\nu} \tag{2.2}$$

Where T_b^{obs} is the observed temperature at a frequency ν, T_{ex} is the cloud uniform excitation temperature, also known as the spin temperature T_S, T_R describes the background radio source temperature and τ_ν is the cloud optical depth.

As previously mentioned, the 21 cm line has a rest frequency $\nu_0 = 1420$ MHz, which corresponds to a brightness temperature T_b. When taking the cosmological redshift into account, the brightness T_b measured in a cloud's comoving frame at redshift z

results in an apparent brightness on Earth of $T_b^{obs}(\nu) = T_b(\nu_0)/(1 + z)$, where the observed frequency is $\nu = \nu_0/(1 + z)$.

After taking the cosmological expansion into consideration and relating the observed and emitted frequencies, the brightness temperature can be expressed in differential form,

$$\delta T_b = \frac{T_S - T_R}{1 + z}(1 - e^{-\tau_\nu}) \tag{2.3}$$

$$\approx \frac{T_S - T_R}{1 + z}\tau \tag{2.4}$$

$$\approx 27x_{HI}(1 + \delta_b)\left(\frac{\Omega_b h^2}{0.023}\right)\left(\frac{0.15}{\Omega_m h^2}\frac{1 + z}{10}\right)^{1/2} \times \left(\frac{T_S - T_R}{T_S}\right)\left[\frac{\partial_r v_r}{(1 + z)H(z)}\right] mK \tag{2.5}$$

Where x_{HI} is the neutral fraction of hydrogen, δ_b is the fractional overdensity in baryons, and the final term arises from the velocity gradient along the line of sight $\partial_r v_r$.

2.1 21 cm Detection

Detecting the 21 cm signal, depends on the spin temperature T_S. In order for this signal to be observable, T_S needs to deviate from the background temperature T_R. The spin temperature can be determined through three processes:

· P_1: Absorption/Emission of 21 cm photons from/to the radio background.

· P_2: Collisions with other hydrogen atoms and with electrons.

· P_3: Resonant scattering of $Ly\alpha$ photons that cause a spin flip via an intermediate excited state.

The spin temperature can be given by the equilibrium balance of these processes, considering that their rate is fast compared the the line's de-excitation time. In this limit, the spin temperature is given by,

$$T_S^{-1} = \frac{T_\gamma^{-1} + x_\alpha T_\alpha^{-1} + x_c T_K^{-1}}{1 + x_\alpha + x_c} \tag{2.6}$$

Where T_γ is the temperature of the surrounding bath of radio photons, usually set by the CMB, so that $T_\gamma = T_{CMB}$; T_α is the color temperature of the $Ly\alpha$ radiation

field at the $Ly\alpha$ frequency and is closely coupled to the gas kinetic temperature T_K, x_c and x_α are the coupling coefficients due to atomic collisions and scattering of $Ly\alpha$ photons, respectively. When $x_{tot} \equiv x_c + x_\alpha \gtrsim 1$, the spin temperature T_S becomes strongly coupled to the gas temperature and when $x_{tot} \ll 1$, T_S relaxes to T_γ.

Radio Background

P_1 process utelises mainly two types of background radio sources when using the 21 cm line as a probe for research:

    1- The Cosmic Microwave Background:

       · $T_R = T_{CMB}$

       · 21 cm feature is seen as a spectral distortion to the CMB blackbody at appropriate radio frequencies.

       · This distortion forms a diffuse background that can be studied across the whole sky.

       · Observations at different frequencies probe different spherical shells of the observable universe, so that a 3D map can be constructed.

    2- Radio loud point source (such as quasars):

       · $T_R \gg T_S$

       · The source is always much brighter than the weak emission from diffuse hydrogen gas.

       · The gas is seen in absorption against the source.

       · Lines from regions of neutral gas at different distances to the source lead to a "forest" of lines known as the "21 cm forest".

       · Due to the high brightness of the background source, the 21 cm forest can be studied with high frequency resolution, allowing to probe small scale structures in the inter galactic medium (IGM).

Collisional Coupling

During the dark ages, when the gas density was high, collisions between different particles induced spin flips in hydrogen atoms and dominated the coupling. The collisions took three paths:

· Between two hydrogen atoms (H-H).

· Between a hydrogen atom and an electron (H-e).

· Between a hydrogen atom and a proton (H-p).

Neutral hydrogen atoms can also collide with bare protons, deuterium atoms, and helium atoms or irons.

Resonant Scattering

Once star formation begins at the cosmic dawn, resonant scattering of $Ly\alpha$ photons, provides a second channel for coupling. This process is known as the Wouthuysen-Field effect. It describes how $Ly\alpha$ photon scattering affects T_S.

2.2   Global Evolution

After having described the physics of the 21 cm line, it is important to understand the evolution of the IGM through time. In order to do so, the IGM will be treated as a two phase medium. Initially, it was composed of a single mostly neutral phase left over after recombination. This phase is where the 21 cm signal is generated and has a gas temperature T_K and a small fraction of free electrons x_e. When galaxy formation begins, energetic UV photons ionize HII regions surrounding, starting with individual galaxies, and then clusters of galaxies. The ionized HII bubbles constitute the second phase in the IGM, characterised by a volume filling fraction x_i. These regions will experience growth, governed by the interplay between ionization and recombination, and they will expand into neutral hydrogen. Figure 2.1 shows the global spin temperature evolution.

During its evolution, the IGM experiences different types of heating, which affects its composition and temperature. At high redshifts, the dominant heating rate mechanism is Compton heating, arising from scattering of CMB photons from the small residual free electron fraction. Compton heating serves to couple T_K to T_γ at redshifts $z \gtrsim 150$, but becomes ineffective below that redshift. At lower redshifts, other sources of heat are seen, triggered by the growth of non-linear structures, such as shocks associated with large scale structures and the scattering of $Ly\alpha$ photons off hydrogen atoms. $Ly\alpha$ heating may be insufficient to heat the gas to the CMB temperature alone as it usually requires large fluxes to do so, as such it is more relevant at later times. The most important source of energy injection into the IGM is via X-ray heating of the gas. Since X-ray photons have a long mean free path, thay are able to heat the gas far from the source, and can be produced in large quantities once compact objects are formed.
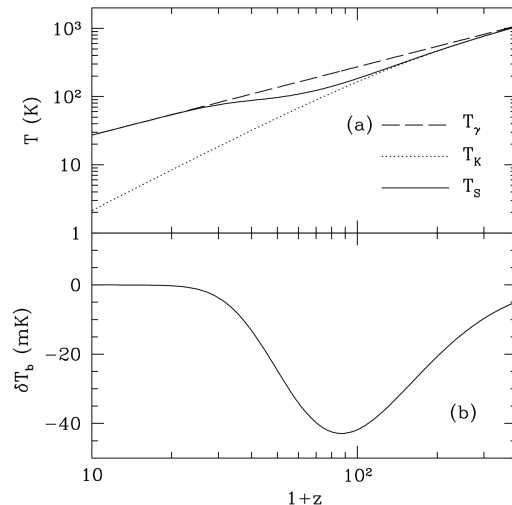
Figure 2.1: IGM temperature evolution if only adiabatic cooling and Compton heating are involved. The spin temperature T_S includes only collisional coupling. (b): Differential brightness temperature against the CMB for T_S shown in panel (a). Source: Steven R. Fulanetto 2006

To determine the 21 cm signal at a given redshift, the four quantities: x_i, x_e, T_K, and J_α must be calculated (J_α being the specific flux calculated at the $Ly\alpha$ frequency). Begining with the evolution of T_K with time,

$$\frac{dT_K}{dt} = \frac{2T_K}{3n}\frac{dn}{dt} + \frac{2}{3k_B}\sum_i \frac{\epsilon_i}{n} \tag{2.7}$$

Where the first term on the right is the pdV work from expansion, and ϵ_i is the energy injected into the gas per second per unit volume through process i.

Next, the volume filling fraction x_i and the ionization of the neutral IGM x_e are considered,

$$\frac{dx_i}{dt} = (1 - x_e)\Lambda_i - \alpha_A C x_i^2 n_H \tag{2.8}$$

$$\frac{dx_e}{dt} = (1 - x_e)\Lambda_e - \alpha_B(T) x_e^2 n_H \tag{2.9}$$

In these expressions, Λ_i is defined as the rate of production of ionizing photons per unit time per baryon applied to HII regions. Λ_e is the equivalent quantity in the bulk of the IGM, $\alpha_A = 4.2 \times 10^{-13} cm^3 s^{-1}$ is the case-A recombination coefficient at $T = 10^4 K$, $\alpha_B(T)$ is the case-B recombination rate, and $C \equiv \langle n_e^2 \rangle / \langle n_e \rangle^2$ is the clumping factor. [1]

As for the evolution of the $Ly\alpha$ flux, it is produced by stellar emission ($J_{\alpha,\star}$) and by X-ray excitation of HI ($J_{\alpha,X}$). Photons emitted by stars, may generate $Ly\alpha$ photons via atomic cascades, so the average $Ly\alpha$ background is,

$$J_{\alpha,\star}(z) = \sum_{n=2}^{n_{max}} J_\alpha^{(n)}(z) = \sum_{n=2}^{n_{max}} f_{recycle}(n) \int_z^{z_{max}(n)} dz' \frac{(1+z)^2}{4\pi} \frac{c}{H(z')} \hat{\epsilon}_\star(v_n', z') \quad (2.10)$$

Where $z_{max}(n)$ is the maximum redshift from which emitted photons will redshift into the level n Lyman resonance, v_n' is the emission frequency at z' corresponding to absorption by the level n at z, $f_{recycle}(n)$ is the probability of producing a $Ly\alpha$ photon by cascade from level n, and $\hat{\epsilon}_\star(v, z)$ is the comoving photon number emissivity for stellar sources.

The $Ly\alpha$ flux ($J_{\alpha,X}$) produced by X-ray excitation may be found by balancing the rate at which $Ly\alpha$ photons are produced via cascades with the rate at which photons redshift out of the $Ly\alpha$ resonance, giving,

$$J_{\alpha,X} = \frac{c}{4\pi} \frac{\epsilon_{X,\alpha}}{h\nu_\alpha} \frac{1}{H\nu_\alpha} \quad (2.11)$$

Ovreview

As previously stated, the 21 cm brightness temperature may be expressed as a function of four variables $T_b = T_b(T_K, x_i, x_e, J_\alpha)$. When calculating the 21 cm signal, a model for the evolution of and fluctuations in these quantities is required. T_b's dependence on each of these quantities saturates at some point, which will lead to the creation of separate regimes each dominated by this dependence. As such, variation in only one of the variables will dominate fluctuations in the signal. These different regimes are shown in schematic form in Figure 2.2 and are shown graphically in Figure 2.3.

· $200 \lesssim z \lesssim 1100$: The residual free electron fraction left after recombination allows Compton scattering to maintain thermal coupling of the gas to the CMB, setting $T_K = T_\gamma$. The high gas density leads to effective collisional coupling so that $T_S = T_\gamma$ and T_b is expected to be 0 and no detectable 21 cm signal.

· $40 \lesssim z \lesssim 200$: In this regime, the gas cools adiabatically so that $T_K \propto (1+z)^2$ leading to $T_K < T_\gamma$ and collisional coupling sets $T_S < T_\gamma$, leading to $T_b < 0$ and
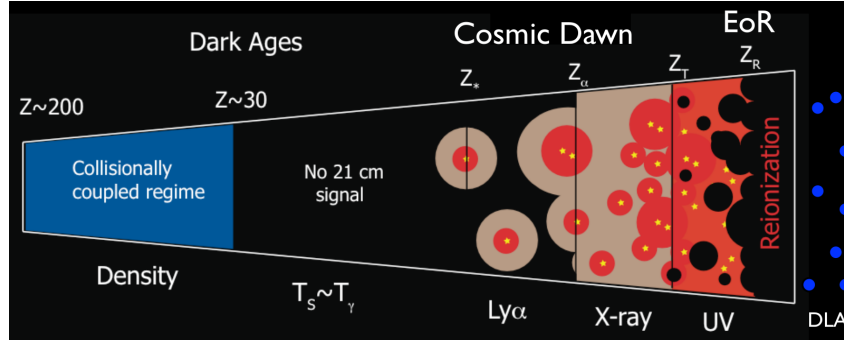
Figure 2.2: Cartoon of the different phases of the 21 cm signal. The signal transitions from an early phase of collisional coupling to a later phase of Ly_α coupling through a short period where there is little signal. Fluctuations after this phase are dominated successively by spatial variation in the Ly_α, X-ray, and ionizing UV radiation backgrounds. After reionization is complete there is a residual signal from neutral hydrogen in galaxies. Source: R.Pritchard 2012

an early absorption signal. At this time, T_b fluctuations are sourced by density fluctuations, potentially allowing the initial conditions to be probed. This marks the earliest epoch for which 21 cm observations are possible.

· $z_\star \lesssim z \lesssim 40$: As the expansion continues, decreasing the gas density, collisional coupling becomes ineffective and radiative coupling to the CMB sets $T_S = T_\gamma$, and there is no detectable 21 cm signal.

The last two epochs that were just stated, define the beginning and end of the Dark Ages for the purpose of the 21 cm line. The remaining transition points are determined by luminous sources, so their timing is much more uncertain.

· $z_\alpha \lesssim z \lesssim z_\star$: Once the first sources switch on at $z_\star$, they emit both $Ly\alpha$ photons and X-rays. In general, the emissivity required for $Ly\alpha$ coupling is significantly less than that for heating T_K above T_γ. The spin temperature is coupled to cold gas which results in $T_S \sim T_K < T_\gamma$ and there is an absorption signal. Fluctuations are dominated by density fluctuations and variation in the $Ly\alpha$ flux. As further star formation occurs the $Ly\alpha$ coupling will eventually saturate ($x_\alpha \gg 1$), so that by a redshift z_α the gas will be strongly coupled everywhere.

· $z_h \lesssim z \lesssim z_\alpha$: After $Ly\alpha$ coupling saturates, fluctuations in the $Ly\alpha$ flux no longer

affect the 21 cm signal. By this point, heating becomes significant and gas temperature fluctuations source T_b fluctuations. While T_K remains below T_γ, a 21 cm signal is seen in absorption, but as T_K approaches T_γ hotter regions may begin to be seen in emission. Eventually by a redshift z_h the gas will be heated everywhere so that $T_K = T_\gamma$.

· $z_T \lesssim z \lesssim z_h$: After the heating transition, $T_K > T_\gamma$ and a 21 cm signal is expected to be seen in emission. The 21 cm brightness temperature is not yet saturated, which occurs at z_T, when $T_S \sim T_K \gg T_\gamma$. Brightness temperature fluctuations are sourced by a mixture of fluctuations in ionization, density and gas temperature.

· $z_r \lesssim z \lesssim z_T$: Continued heating drives $T_K \gg T_\gamma$ at z_T and temperature fluctuations become unimportant. By this point, the filling fraction of HII regions probably becomes significant and ionization fluctuations begin to dominate the 21 cm signal.

· $z \lesssim z_r$: After reionization, any remaining 21 cm signal originates primarily from collapsed islands of neutral hydrogen.

Figure 2.4 shows different models of the global 21 cm signal and the associated evolution in the neutral fraction and gas temperatures. Each model assumes different conditions for initial star formation, which leads to different scenarios of IGM evolution. At high redshift, the gas temperature cools adiabatically faster than the CMB. At the same time, collisional coupling is effective at coupling spin and gas temperatures leading to the absorption trough seen at the right of the lower panel. Collisional coupling starts to become ineffective at the minima of this through. Once star formation begins, the spin and gas temperatures again become tightly coupled leading to a second deeper absorption trough.
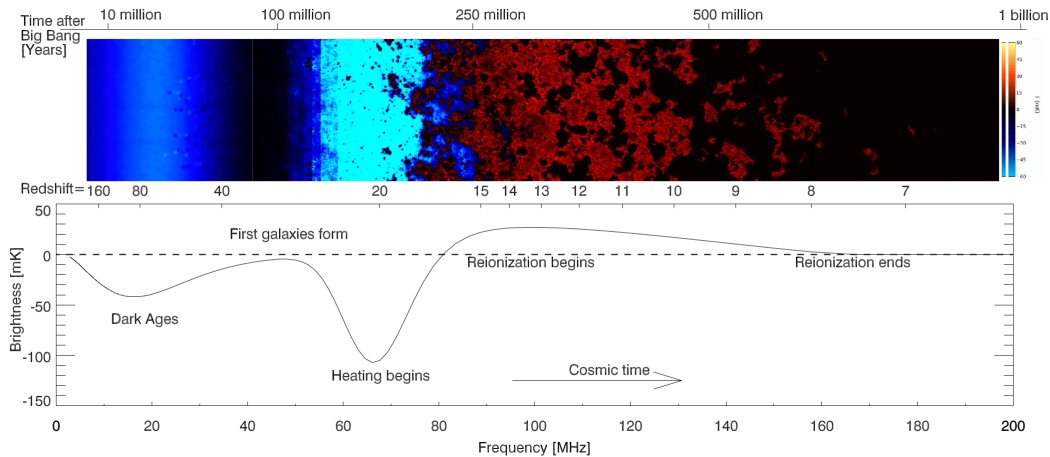
Figure 2.3: The 21 cm cosmic hydrogen signal. (a) Time evolution of fluctuations in the 21-cm brightness from just before the first stars formed through to the end of the reionization epoch. This evolution is pieced together from redshift slices through a simulated cosmic volume. Coloration indicates the strength of the 21-cm brightness as it evolves through two absorption phases (purple and blue), separated by a period (black) where the excitation temperature of the 21-cm hydrogen transition decouples from the temperature of the hydrogen gas, before it transitions to emission (red) and finally disappears (black) owing to the ionization of the hydrogen gas. (b) Expected evolution of the sky-averaged 21-cm brightness from the "dark ages" at redshift 200 to the end of reionization, sometime before redshift 6 (solid curve indicates the signal; dashed curve indicates $T_b = 0$). The frequency structure within this redshift range is driven by several physical processes, including the formation of the first galaxies and the heating and ionization of the hydrogen gas. There is considerable uncertainty in the exact form of this signal, arising from the unknown properties of the first galaxies. Source: R.Pritchard 2012

2.3 The Power Spectrum & 21 cm Tomography

The 21 cm intensity field resulting from the reionization process is described using the power spectrum of 21 cm fluctuations. Each and every component of the brightness temperature fluctuates significantly. Types of fluctuations:

· Density fluctuations: From evolution of the cosmic web.

· 21 cm fluctuations: From different types of luminous sources.

The advantage of the 21 cm line is that it allows to separate this fluctuating component both on the sky and in frequency. Thus detailed studies can be made on the sources and their effects on the IGM by doing "tomographic" observations.

Defining the fractional perturbation to the brightness temperature: $\delta_{21}(x) \equiv [\delta T_b(x)-$
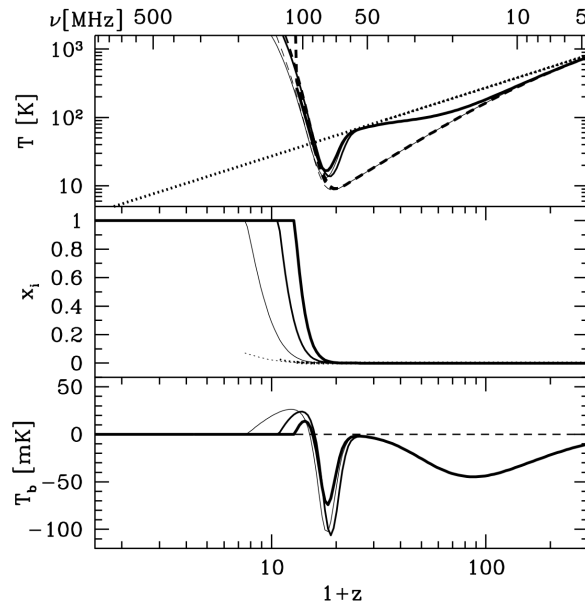
Figure 2.4: Top panel: Evolution of the CMB temperature T_{CMB} (dotted curve), the gas kinetic temperature T_K (dashed curve), and the spin temperature T_S (solid curve). Middle panel: Evolution of the gas fraction in ionized regions x_i (solid curve) and the ionized fraction outside these regions (due to diffuse X-rays) x_e (dotted curve). Bottom panel: Evolution of mean 21 cm brightness temperature T_b . In each panel we plot curves for model A (thin curves), model B (medium curves), and model C (thick curves). Source: R.Pritchard 2012

$\delta T_b]/\delta T_b$. The fourier transform of the previous expression $\tilde{\delta}_{21}(k)$ is of great importance, and it's power spectrum is,

$$\left\langle \tilde{\delta}_{21}(k_1)\tilde{\delta}_{21}(k_2) \right\rangle \equiv (2\pi)\pi^3 \delta_D(k_1 + k_2)P_{21}(k_1) \tag{2.12}$$

Where $\delta_D(x)$ is the Dirac delta function. Usually, the power spectrum $P(k)$ is the 3D Fourier transform of the corresponding 2D function. As previously shown (equations 2.6 and 2.7) , the brightness temperature depends on multiple parameters. Expanding the fluctuations to linear order,

$$\delta_{21} = \beta\delta_b + \beta_x\delta_x + \beta_\alpha\delta_\alpha + \beta_T\delta_T - \delta_{\partial v} \tag{2.13}$$

Where each δ_i describes the fractional variation in a particular quantity: δ_b for the baryonic density, δ_α for the $Ly\alpha$ coupling coefficient x_α , δ_x for the neutral fraction δ_T for T_K, and $\delta_{\partial v}$ for the line-of-sight peculiar velocity gradient. The expansion coefficients β_i are given by,

$$\beta = 1 + \frac{x_c}{x_{tot}(1 + x_{tot})} \tag{2.14}$$

$$\beta_x = 1 + \frac{x_c^{HH} - x_c^{eH}}{x_{tot}(1 + x_{tot})} \tag{2.15}$$

$$\beta_\alpha = \frac{x_\alpha}{x_{tot}(1 + x_{tot})} \tag{2.16}$$

$$\beta_T = \frac{T_\gamma}{T_K - T_\gamma} + \frac{1}{x_{tot}(1 + x_{tot})} \left(x_c^{eH} \frac{dln\kappa_{10}^{eH}}{dlnT_K} + x_c^{HH} \frac{dln\kappa_{10}^{HH}}{dlnT_K} \right) \tag{2.17}$$

Where $x_{tot} \equiv x_c + x_\alpha$ and the collisional term is split into the dominant H-e and H-H components (x_c^{eH} and x_c^{HH}, respectively).

From the above, the power spectrum can be constructed as follows,

$$
\begin{aligned}
P_{T_b}(k, \mu) = \quad & P_{bb} + P_{xx} + P_{\alpha\alpha} + P_{TT} + 2P_{bx} \\
& +2P_{b\alpha} + 2P_{bT} + 2P_{x\alpha} + 2P_{xT} + 2P_{\alpha T} \\
& +P_{x\partial x\partial} + \text{other quartic terms} \\
& +2\mu^2(P_{b\partial} + P_{x\partial} + P_{\alpha\partial} + P_{T\partial}) \\
& +\mu^4 P_{\partial\partial} \\
& +2P_{x\partial\partial_{\delta v}x} + P_{x\delta_{\partial v}\delta_{\partial v}x} \\
& + \text{other quartic terms with } \delta_{\partial v} \tag{2.18}
\end{aligned}
$$

Also to be taken into account during analysis of the power spectrum are the redshift-space distortions, and the ionization and coupling fluctuations. (**2**)

Figure 2.5 shows how the power spectrum evolves as a function of redshift for several fixed k-values. Four epochs stand out in this figure. For $z \gtrsim 30$ the power spectrum has a peak at $z \approx 50$. At the begining of star formation, coupling and temperature fluctuations become noticable resulting in a complicated evolution. The next phase is where ionization fluctuations dominate, resulting in the loss of signal at the end of reionization. Finally, a weak signal emerges from the left over neutral hydrogen in dense clumps which grows as structures continue to collapse.

Measuring the global 21 cm signal can be done by using the absolute temperature measurements as a function of frequency, averaged over the sky. Considering that the signal is constant over different large patches of the sky, measuring it does not need
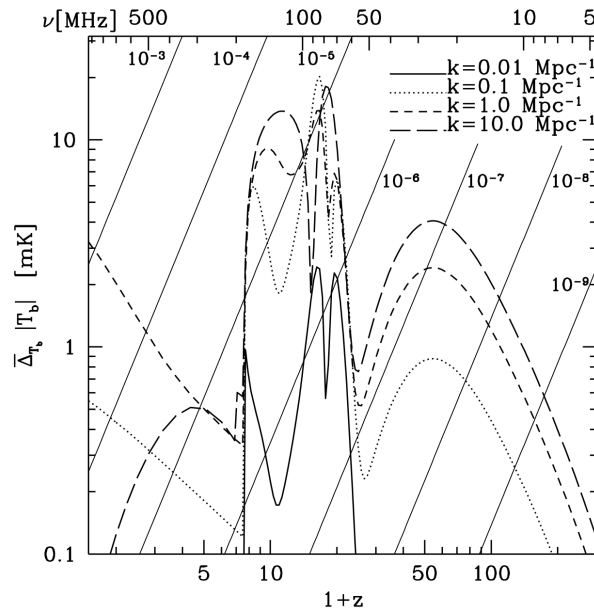
Figure 2.5: Evolution of power spectrum fluctuations. The different curves show $P(k, z)$ as a function of z at fixed k for $k = 0.01, 0.1, 1, 10 Mpc^{-1}$. Diagonal lines show $\epsilon T_{fg}(\nu)$, the foreground temperature reduced by a factor ϵ ranging from $10^{-3} - 10^{-9}$ to indicate the level of foreground removal required to detect the signal. Source: R.Pritchard 2012

high angular resolution and can be carried out with just a single dipole. However, the measurement is complicated by the need to remove galactic foregrounds, which are much larger than the desired signal. Foreground removal thechniques should result in spectral smoothness of the foregrounds in contrast to the frequency structure of the signal.

Probing the Dark ages ($1100 > z > 40$) might be a great challenge at the moment considering the huge amount of foreground removal needed at such low frequencies ($T_{sky} \sim 10^5$ K at 15 MHz). However the fluctuating 21 cm signal might still be observable, providing a probe of the primordial matter power spectrum over a wide range of scales. An advantage of 21 cm observations is the immense amount of samples available ($\sim 6 \times 10^{11}$ patches with 1 Mpc radii for $100 > z > 30$). The line from the epoch of reionization (EoR) is redshifted to meter wavelengths which requires radio frequency detectors. In this case, an interferometer composed of many dipole anntenae is the ideal design for 21 cm observations. In order to synthesis a beam on the sky, signals from individual dipoles need to be cross-correlated. The details of such a detector are the subject of the next chapter.

Chapter 3

THE ANTENNA

As previously discussed, the Dark Ages, ranging between $z = 1100$ and $z = 40$, exhibits an emission of 21 cm signal at $40 < z < 200$. During this period, the received frequency range is 7 MHz $< v < 35$ MHz (using $v = v_0/(1 + z)$ from chapter 2). The deployed antennae should be able to pick up these frequencies in order to porperly study this period in the development of the universe. The fluctuations during and before the epoch of reionization require low frequency telescopes with baselines of kilometric order to acheive sufficiently good angular resolution.

In low frequency telescopes, the best achievable angular resolution θ_D depends on the largest dimension D_{max} of the telescope, $\theta_D \sim \lambda/D_{max}$. In the case of the 21 cm signal, $\theta_D \sim \lambda_0(1 + z)/D_{max}$, where $\lambda_0 = 21.1$ cm. The value of θ_D depends on aperture illumination, the type of the telescope, and procedures used for calibration and image processing. An estimated value of the redshifted 21 cm line is $\theta_D \sim 1.2°[(1 + z)/10](D_{max}/100m)^{-1}$. Dipole arrays can be used to get the required large collecting areas. This collecting area will dictate the detectability of distant radio sources having angular sizes less than θ_D.

The telescope sensitivity depends on both the strength of the collected signal by the antenna and the noise, which can have different origins. Most of the noise source in radio telescopes is from the first amplifiers connected to the output of the antenna. The celestial signal strength and the receiver noise level are best compared at the electrical junction between the antenna and the first amplifier. The output signal of the antenna can be described as the antenna temperature T_a which is the temperature of a matched resistive load. The power produced by that temperature ($P_a = k_B T_a \Delta v$ for the resistor) is the same as the signal power $P = A_e S_v \Delta v/2$ received in one of two orthogonal antenna polarizations (with S_v being the source flux density, Δv the observed bandwidth, and A_e the effective collecting area of the telescope). As such the antenna sensitivity factor can be defined as $K_a = T_a/S_v = A_e/2k_B$ in KJy^{-1}.

Defining the system temperature T_{sys} as the temperature of a standard resistor input to an ideal noise-free receiver, producing the same noise power level as measured at the output of the actual receiver; the signal to noise ratio is computed by comparing

T_{sys} and T_a. Aslo defining the radiometer equation,

$$\Delta T^N = \kappa_c \frac{T_{sys}}{\sqrt{\Delta \nu \, t_{int}}} \approx \frac{T_{sys}}{\sqrt{\Delta \nu \, t_{int}}} \qquad (3.1)$$

Where $\kappa_c \geqslant 1$ is a loss factor which depends on the details of the signal detection scheme.

3.1 The Radio Sky

When the antennae are pointed to an area of the sky that has a brightness temperature T_{sky}, the received noise power will increase such that $T_{sys} \geqslant T_{sky}$. Fore 21 cm line detection, the relevant low radio frequencies correspond to a sky that is so bright that $T_{sys} \approx T_{sky}$. T_{sky} is dominated by synchrotron radiation from fast electrons in the Milky Way. In general, for typical high altitude "quiet" portions of the sky,

$$T_{sky} = 16.3 \times 10^6 K \left(\frac{\nu}{2 \, MHz} \right)^{-2.53} \quad at \; \nu > 2MHz. \qquad (3.2)$$

The obvious conclusion from the above, is that the foregrounds are several orders of magnitude larger than the expected signal. So the challenge will be to separate the cosmological components, which can be done by using large collecting areas. In order to minimize T_{sky}, the selected viewing areas must be chosen so as to have small sky brightness. For this research, the dark side of the moon is chosen, where it is shielded from the earth's and sun's radiations.

3.2 Telescope Sensitivity

The sensitivity of compact sources that are unresolved by the diffraction limited beam θ_D of the array can be easily computed. Starting with the noise level,

$$\sigma_S = \frac{T_{sys}/K_a}{\sqrt{\Delta \nu \, t_{int}}}, \qquad (3.3)$$

Where K_a includes the total effective collecting area of the telescope.

When the telescope is made of an array of small apertures, the sensitivity of radio telescopes can be confused with low surface brightness features. The equivalent brightness temperature uncertainty can be obtained by using a relation between brightness temperature and flux density,

$$\Delta T^N = \frac{\sigma_S c^2}{2k_B \nu^2 \Omega_B} \tag{3.4}$$

Where the telescope beam delimits a solid angle $\Omega_B \approx \theta_D^2$ if its collecting area is ditributed over an area of diameter D. Using the definitions of σ_S, K_a and θ_D, equation (3.4) reduces to,

$$\Delta T^N = \left(\frac{D_{max}^2}{A_{tot}}\right) \frac{T_{sys}}{\sqrt{\Delta \nu \, t_{int}}} \equiv \frac{T_{sys}}{\eta_f \sqrt{\Delta \nu \, t_{int}}} \tag{3.5}$$

Where A_{tot} is the total effective area and $\eta_f \equiv A_{tot}/D_{max}^2$ is the array filling factor. In order to achieve better angular resolution, the total collecting area is spread over large areas which means that the integration time required to detect a given surface brightness grows as $t_{int} \propto D_{max}^4$.

For large collecting areas, the array dilution factor η_f substantially decreases the sensitivity. For an interferometric array, using equation 3.2, for the system temperature,

$$\Delta T^N|_{int} \sim 2mK \left(\frac{A_{tot}}{10^5 m^2}\right) \left(\frac{10'}{\Delta \theta}\right)^2 \left(\frac{1+z}{10}\right)^{4.6} \left(\frac{MHz}{\Delta \nu} \frac{100 \, hr}{t_{int}}\right)^{1/2} \tag{3.6}$$

The effective collecting area at a given angular resolution actually depends on the distribution of baselines in the array. As such, careful attention must be paid to antenna placement during array design.

3.3 Interferometer Response Patterns

In an interferometer, the combined response projected on the sky of two electronically coupled antennae, resembles the characteristic diffraction pattern from a double slit. The interferometer response to the sky brightness distribution $I_\nu(\hat{n})$ is,

$$\int d\Omega I_\nu(\hat{n}) E_1(\hat{n}_0, \hat{n}, \nu) E_2^*(\hat{n}_0, \hat{n}, \nu) e^{2\pi i \hat{n}.B/\lambda} \tag{3.7}$$

Where $E_i(\hat{n}_0, \hat{n}, \nu)$ is the complex electric field response pattern of the ith element. In the term $\exp(2\pi i \hat{n}.B/\lambda)$, B is the baseline vector from one interferometer element to the other. Assuming that all elements have identical beam patterns, the primary beam power pattern $W_\nu(\hat{n}_0, \hat{n})$ is the product of the electric field patterns. In radio

astronomy, the response for a particular "visibility" V, corresponding to a particular baseline and frequency pair, in units of flux density is,

$$V_{Jy}(B, \hat{n}_0, \nu) = \frac{2k_B}{\lambda^2} \int d\Omega \delta T_b(\hat{n}, \nu) W_\nu(\hat{n}_0, \hat{n}) e^{2\pi i \hat{n}.B/\lambda} \qquad (3.8)$$

This is the standard equation for describing aperture synthesis techniques, considering that radio interferometer arrays are designed to sample V at many coordinates and then reconstruct images of the sky through the inverse Fourier integral.

3.4   Foreground Removal

As previously mentionned, foregrounds, mostly the mean brightness temperature of our Galaxy, are huge at such low radio frequencies. On the other hand, only the fluctuations on the sky of this large mean brightness are of interest. CMB foreground studies suggests that galactic fluctuations will be relatively gentle on arcminute scales. However, even if these fluctuations are small, the 21 cm signal is still saturated by temperature fluctuations from radio galaxies, and free-free emission from the reionizing sources. Both of these fluctuations exceed the signal by a couple of orders of magnitude.

Luckily, it is possible to recover the 21 cm signal through its structure in frequency space, considering that all the previously mentioned foreground contaminants are spectrally smooth. More elaborately, while the 21 cm signal is expected to be somewhat isotropic in 3D space, foregrounds have strong fluctuations in the transverse direction across the sky but weak ones in the radial direction.

The strong frequency coherence of foregrounds is mainly used for cleaning the signal. These foregrounds could be easily removed if they were perfect power laws. Unfortunately, the galactic foreground spectral index fluctuates as a function of both frequency and position and extragalactic foregrounds are a sum of power law spectra with different spectral indices, which in general won't result in a power law. This is what limits the efficacy of foreground removal. Although the 21 cm signal exhibits a 3D nature, foreground removal is better understood with the angular power spectrum, because that separates the angular power spectrum (which is contaminated) from the much cleaner spectral fluctuations used for cleaning.

Finally, foreground removal depends on the details of one's application and on the properties of array design; as such they are best addressed in end-to-end simulations where full error probability distributions and biases can be carefully quantified. (**3**)

3.5 Antenna Design

Different antenna designs are available for the task at hand (Dish antenna, single dipoles,...). However, the most efficient design for this specific detection of the 21 cm line, entailes an aperture synthesis interferometric array implemented with a swarm of nano-satellites where each satellite carries an element of the array. The cosmic signal received by a large number of time-varying antenna positions, is combined to produce high quality sky maps. For a N-antenna array, each antenna pair forms a baseline of an aperture synthesis interferometer, contributing $\bar{N} \triangleq 0.5N(N-1)$ unique sampling points at a given time instant. If $x_i(t)$ and $x_j(t)$ are two arbitrary antenna position vectors at time t forming a baseline, then the corresponding uvw point is,

$$[u_{ij}(t), v_{ij}(t), w_{ij}(t)]^T \triangleq (x_i(t) - x_j(t))/\lambda \qquad (3.9)$$

Where λ is the observed wavelength. Figure 3.1 shows the uvw points in blue for a $N = 9$ satellite cluster which is arbitrarily deployed with a maximum distance separation of $d = 50$ km and an observational frequency of 10 MHz. The effective synthesized aperture is obtained by projecting the uvw points onto a 2D plane which is orthogonal to the source direction. Three such projections (in black) are shown in figure 3.1, for sources orthogonal to the uv, uw and wv planes.

As previously mentioned, the dominant foreground in the low frequency radio sky is the galactic synchrotron radiation. This emission from electrons causes the brightness temperature to rise from $\sim 10^4$K at 30 MHz, to as high as $\sim 10^7$K around 2 MHz. At frequencies below 2 MHz, the galactic plane is nearly completely opaque and extragalactic sources cannot be observed. Furthermore, expanding on equation 3.3 for a 1 σ RMS sensitivity of an antenna array of N nodes,

$$\sigma_S = \frac{235.6T_{sys}}{\lambda^2\sqrt{N(N-1)(t_{int}/1\ hr)(\Delta v/1MHz)}}\ mJy/beam \qquad (3.10)$$

Where N is the total number of estimated sources above this sensitivity and is given by,

$$N(\sigma) = 1800(\sigma/10mJy)^{-0.3}(v/10\ MHz)^{-0.7} \qquad (3.11)$$

Furthermore, the scattering in the ISM obstructs observational frequencies less than 30 MHz, limiting the maximum baseline between the satellites to,

(a) uvw: Snapshot	(c) uvw: Bandwidth synthesis	(e) uvw: Complete orbit
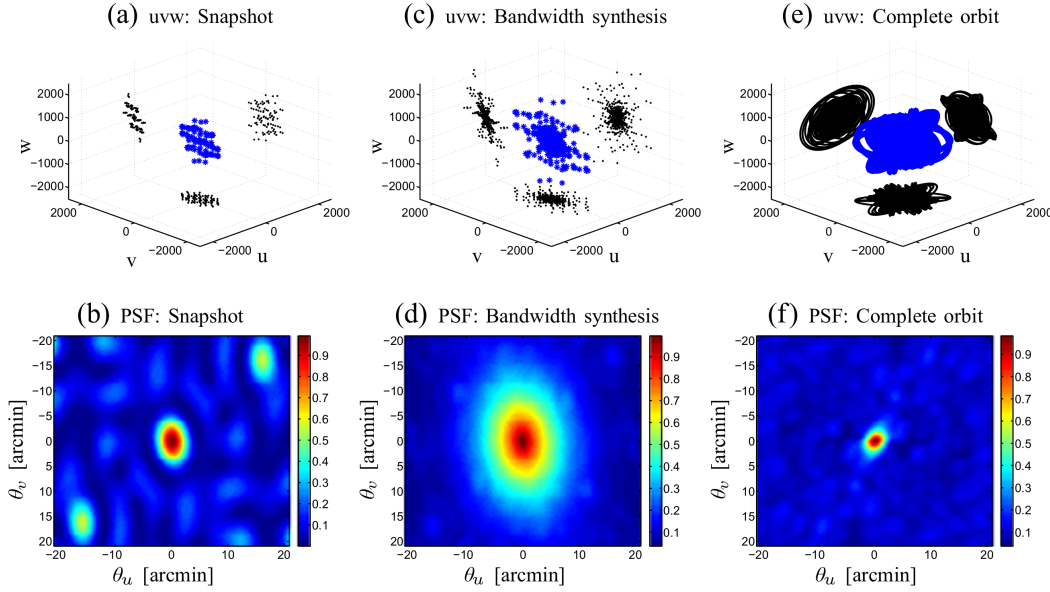
Figure 3.1: Baseline and sky map simulations: Aperture filling of a 9-satellite ULW (Ultra Long Wavelength) array for an Earth leading orbit around the Sun, to illustrate the effect of the sampling space on the normalized Point Spread Function (PSF). The uvw coverage for the 3-D array of satellites at $\nu = 10$ MHz (a) for a single snapshot $N_t = 1$ along with (b) corresponding PSF. Bandwidth synthesis is illustrated in (c) which shows the uvw coverage of single snapshot using 10 frequency bins uniformly distributed in the range 1 - 10 MHz with (d) the resultant PSF. The subfigures (e) and (f) show the UVW and corresponding PSF, for an entire orbit around the sun at 10 MHz with a single observation each day, i.e., 365 snapshots. Source: Raj Thilak Rajan 2016.

$$d_{ISM} = 47 km \times (\nu/1\, MHz)^{1.2} \tag{3.12}$$

Howerver, the lower limit of acheivable noise is the confusion limit and not the RMS sensitivity of the array. Unresolved sources with individual flux densities below the detection limit, lead to a constant noise floor, that is reached after a certain observation time t_{obs}. For extragalactic observations, the anticipated confusion limit due to background sources is,

$$S_{conf}(\theta, \nu) = 16\, mJy \times (\theta/1')^{1.54}(\nu/74\, MHz)^{-0.7} \tag{3.13}$$

Where θ is the effective resolution for which the flux is below the confusion limit. This limit is the lower limit to the acheivable noise floor and as such is an upper limit to the useful collective area of the array. Moreover, the addition of antennas will

only decrease the time in which the confusion limit is reached, but not the overall sensitivity of the array. The time needed for an array to reach this confusion limited sensitivity is given by the "survey equation", (**4**)

$$t_{survey} = 3.3(N/100)^{-2}(10\nu/\Delta\nu)(\nu/1MHz)^{-0.66}(\theta/1')^{-3.08} \qquad (3.14)$$

Using the above, a preliminary design for a space-based array can be acheived, depending on the science case.

	Dark Ages	Galactic discrete	Galactic diffuse emissions	Extra-galactic sources	Solar-terr. physics, transient	Generalized requirement
Science products	global sky signal spectra	sources	all-sky map		triggered observation	all
Freq. Range (MHz) *main cases* *cross ref.*	10 – 30 10 – ≥ 50		1 – 30 1 – ≥ 50		FoV 0.5 – 30 0.1 – ≥ 50	0.5 – 30 0.1 – ≥ 50
Instant. Bandwidth (MHz)	30, 1 for calibration		1		≤ 30	≤ 30
Spectral resolution (kHz)	10^3, 1 for calibration		10^3		0.1 – 10	0.1 – 10^3
Spatial *FoV* *resolution*	$4\pi\ sr$ $4\pi\ sr$		$4\pi\ sr$ $10'$@ 1 MHz, $1'$@ 10 MHz		$4\pi\ sr$ $1' - 5'$	$4\pi\ sr$ 1' $- 4\pi\ sr$
Sensitivity	5 mK in 8 months		100 mJy @ 10 MHz and 5.6 Jy @ 1 MHz		varying	varying
Temporal Resolution	1 min – 8 months		in a yr 1 month		0.01 – 60s	varying
Polarization	I, FS for calibration	I, FS	I	I, FS	FS	FS

(1) Due to lunar sky-blocking, instantaneous $FoV < 4\pi\ sr$;
(2) 10^6Jy is a typical sensitivity level at 15 MHz with a bandwidth of 10^3 kHz for a normal solar burst.
(3) I is intensity, FS denotes full Stokes.

Table 3.1: Science requirements; I is intensity, FS denotes full stokes. Source: Linjie Chen 2018.

Table 3.1 summarizes the requirements to the radio astronomy instrumentation of the DSL (Decameters Space Linear array) mission for various science tasks, which is quit similar to this project's needs and tasks.

DSL, a joint Chinese European mission consists of a mother ship and eight daughter satellites in near identical low altitude lunar orbits. The nine satellites form a linear array, filling the observational aperture in each orbit. Table 3.2 shows the technical requirements for the onboard antenna system.

Frequency range	$1 - 30\,\text{MHz}$
Instantaneous bandwidth	$\geq 1\,\text{MHz}$
Spectral resolution	$\geq 1\,\text{kHz}$
System noise level	$N_{rec} < 10\% N_{sky}$
Number of independent polarization measures	≥ 2
Mass	$< 2\,\text{kg}$
Power consumption	$< 4\,\text{W}$

Table 3.2: Antenna system requirements. Source: Linjie Chen 2018.
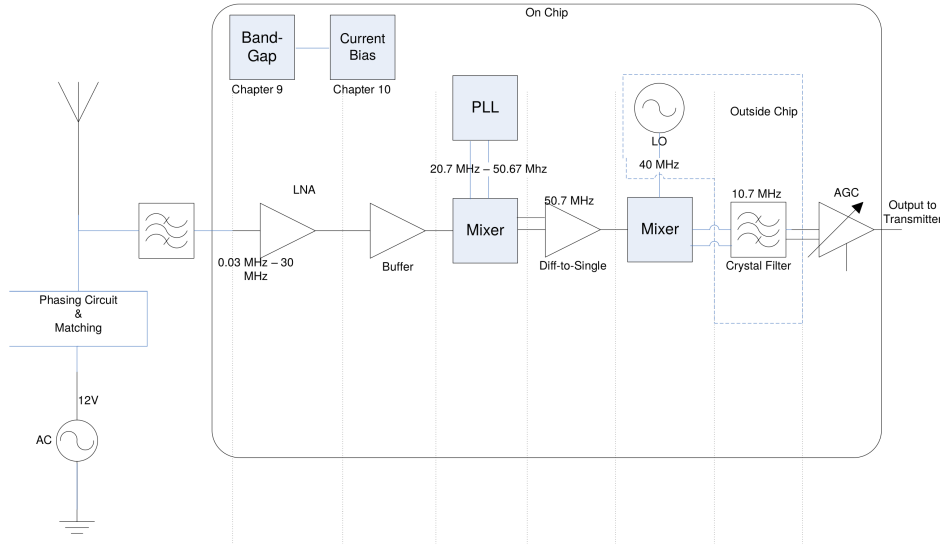
Figure 3.2: Overview of the system.

A complete overview of the system can be seen in figure 3.2, and a more compact one in figure 3.3, having an antenna followed by a low noise amplifier (LNA) and receiver. The different components in figure 3.2 (the buffer, the PLL (phase locked loop), the mixer, the differential to single ended amplifier,the filter, the local oscillator, and the automatic gain control) form the receiver part of the system and are shown for quantitative purposes in this research. As the LNA noise is dominant over the noise of the electronics, the receiver noise is considered negligible in order to simplify the noise analysis of the system. The noise induced on the antenna includes the thermal noise of the antenna and the noise from the sky. At the interface between the antenna and the LNA input, the antenna temperature T_a is given by,

$$T_a = \eta T_{sky} + (1 - \eta)T_0 \tag{3.15}$$

Where η is the radiation efficiency and is always less than 1 due to the ohmic losses of the antenna, and T_0 is the physical temperature of the antenna (chosen as 290 K).
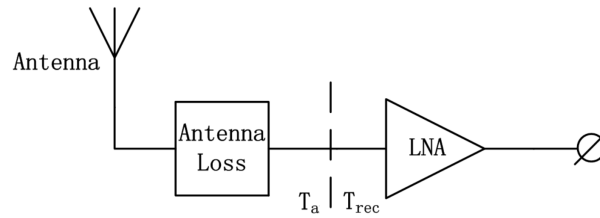
Figure 3.3: Noise model of an antenna with preamplifier. Source: Raj Thilak Rajan 2016.

T_{sky} can take the value given in equation 3.2, and T_{LNA} the LNA noise temperature defined at the input of the LNA is equal to $(1 - \eta)T_0$.

Considering the above discussion, the constraint on the LNA noise temperature is derived as,

$$T_{LNA} < 0.1\eta T_{sky} - (1 - \eta)T_0 \tag{3.16}$$

The Antenna
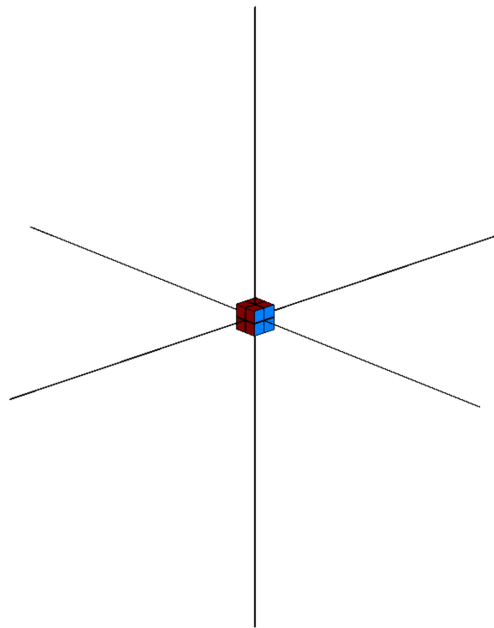
Figure 3.4: Scale model of a tripole antenna (5.0 m) on a micro-satellite (30 × 30 × 30 cm). Source: Raj Thilak Rajan 2016.

As the observational wavelenghts are much larger compared to the dimensions of the satellites, thus due to practical limitations, the realized dipole will be short

compared to the wavelength. The classic half-wave dipole for 10 MHz and 30 MHZ observation frequencies yields a dipole length of 15 m and 10 m respectively. Matched dipoles can be used to maximize the receiver power, but doing so for short dipoles leads to a highly resonant network, significantly limiting the acheivable bandwidth of the system. As such, non-matched dipoles are used; where the LNA noise increases due to the bias mismatching. The required LNA noise is above 10^3 K below 10 MHz and no less than 10^2 K between 10 MHz and 30 MHz even if the antenna is badly mismatched. Although non-matched dipoles have low overall efficiency, they are still able to operate at the sky-noise limited operation over a broad frequency band.

The antenna used for this specific project will be a tripole antenna (figure 3.4). Technically, two cross-dipole antennas are sufficient to get all the polarization information of the cosmic signal. However, adding another orthogonal dipole will increase the detection capability, improve the directivity of the antenna and thereby increase the field of view (FoV). A tripole antenna can also protect against any interference signal, and is capable of estimating the directions of arrival (DOA) of incident signals without spatially distributed arrays, enabling the localization of discrete radio sources.

Similar to the beam forming concept, the induced signal on each dipole of the tripole antenna can be multiplied by a complex weight, and then combining them to get a desired beam. Figure 3.5 shows the usefulness of this property for radio interference supression.

The antenna is simulated onboard a cube sate to evaluate its performance. The three dipoles, mounted in the three orthogonal directions of the cube, are modeled as copper strips having width of 8 mm and thickness of 0.12 mm. The dipole length ranges from 5 to 15 meters. The simulated impedance of a single dipole is shown in figure 3.6, where the resonance frequency of the antenna can be seen to decrease with the increase of its length. A resonance frequency of 15 MHz is needed to acheive the frequency range from 1 to 30 MHz. Nevertheless, the sky noise is dominant at low frequencies, which increases the system temperature and reduces the antenna sensitivity. Thus resonance frequency should be adjusted to optimize antenna performance especially for dark ages study where high sensitivity is needed. By increasing the resonant frequency to 20 MHz, a trade-off is made between the sensitivity and frequency band, whereas the former is improved and the latter is decreased. For this resonant frequency, the corresponding antenna length is 7.5 m.
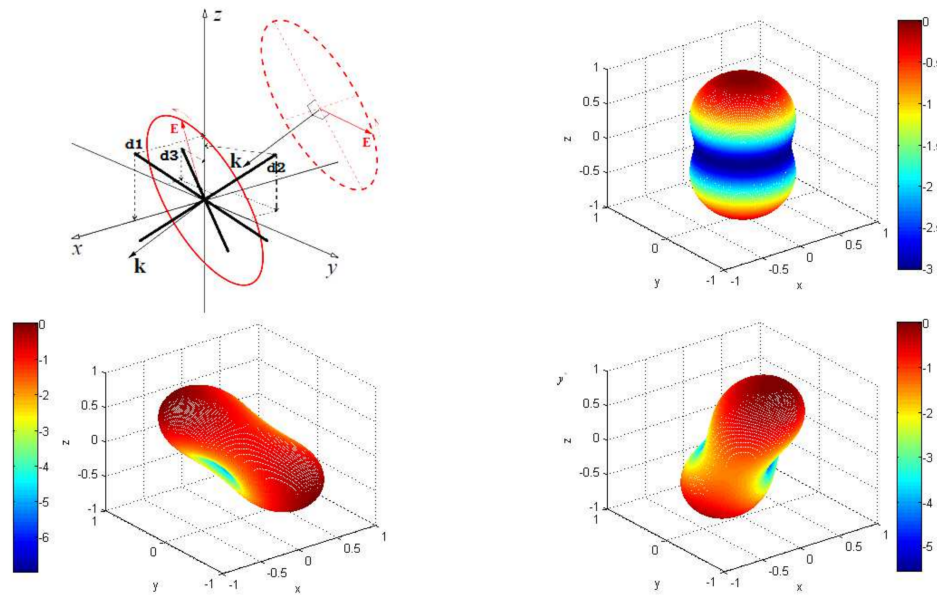
Figure 3.5: Radiation patterns of a tripole antenna in a coordinate system shown in upper left panel for different excitations. The three dipoles of this tripole antenna are placed symmetrically around z axis, the angles between all three dipoles and xy plane are the same, 35.3°. In this case, all these three dipoles are mutually orthogonal and have the same conditions with respect to xy plane. Upper right: $A_1 = 1, A_2 = 1, A_3 = 1. \theta_1 = 0, \theta_2 = 2\pi/3, \theta_3 = -2\pi/3$. Bottom left: $A_1 = 2, A_2 = 0, A_3 = 1.$ $\theta_1 = \pi/6, \theta_2 = 0, \theta_3 = -\pi/3$. Bottom right: $A_1 = 1, A_2 = 2, A_3 = 1.$ $\theta_1 = 0, \theta_2 = 2\pi/3, \theta_3 = -3\pi/4$. Here, A_1, A_2, A_3, and $\theta_1, \theta_2, \theta 3$ indicate respectively the amplitudes and phases of the excitations applied on the three dipoles d1, d2 and d3. Source: Raj Thilak Rajan 2016.

(5)

The LNA

The low noise amplifier which is directly connected to the terminal of the antenna, is an essential component of the system, as it amplifies the induced signal on the antenna without introducing much self-noise. It also serves as a converter, providing a balanced output for unbalanced signals.

The large variation in impedance seen in figure 3.6 makes it difficult to acheive noise matching between LNA and the antenna for large frequency ranges. Having an LNA with a very high input impedance (voltage amplifier) resolves this issue, without the need for coupling between antennas, considering the large amount of electronic circuits onboard the satellite. An antenna with high impedance magnitude, exhibits high current noise. In order to decrease this noise as much as possible, a special type
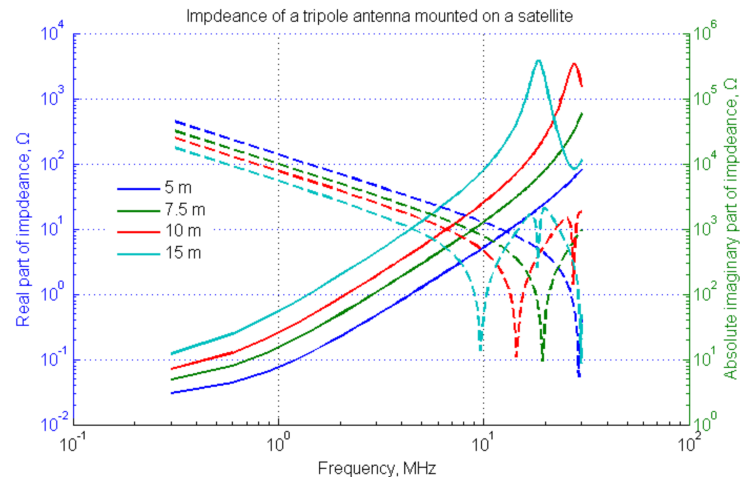
Figure 3.6: Impedance of a tripole antenna onboard a micro-satellite. The solid lines and dashed lines represent real and imaginary parts, respectively. Source: Raj Thilak Rajan 2016.
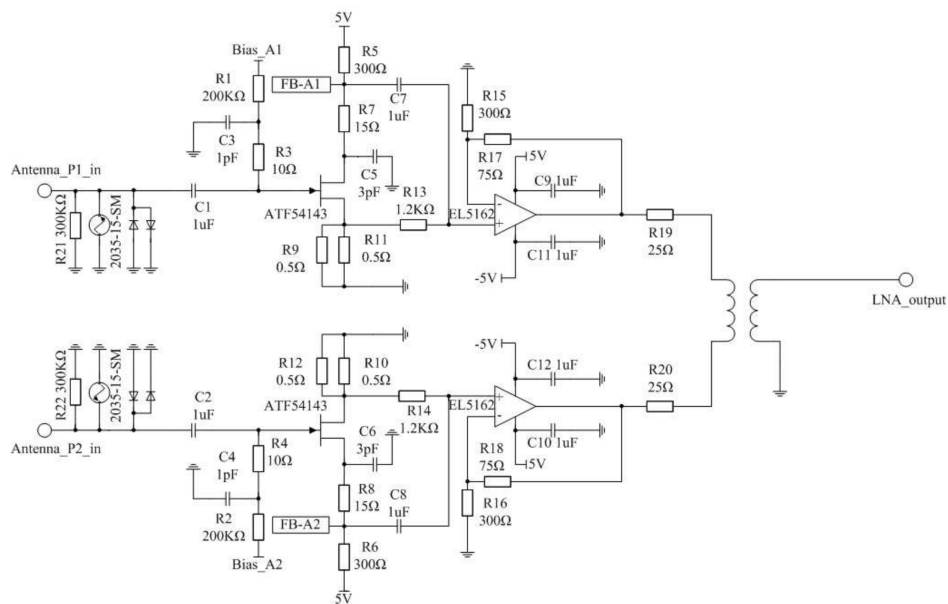
Figure 3.7: Schematic of the low noise amplifier. The blocks FB-A1 and FB-A2 denote the feedback circuits of the first stage. Here the Electro-Static discharge (ESD) protection circuits are designed in the front of the first stage to efficiently decrease the voltage that can damage the E-PHEMT while keeping the input capacitance low in respect to the antenna capacitance. Source: Raj Thilak Rajan 2016.

of transistor (PHEMT: Pseudomorphic high electron mobility transistor) is used.

Figure 3.7 shows the circuit schematic of the low noise amplifier. It is designed as a two stage amplifier: The input signal is amplified by the first stage, and the feedback circuit improves the stability of the amplifier.

The LNA should have a gain of 28 dB with ranges between 20 dB and 40 dB over the entire frequency range.

3.6 Antenna Simulation

In order to have a better grasp on the properties of the antenna and its field patterns, a simulation was conducted for three different lengths (5 m, 7.5 m, 15 m) of the tripole using the software 4nec2.

The antennae used were copper wires having diameter 0.55 mm^2, equivalent to the area of the previously mentioned 8 mm x 0.12 mm strip wire. The selected frequency was 20 MHz, equivalent to the resonant frequency previously discussed in the antenna subsection. Three wires were inserted orthogonal to each other (figure 3.8). A voltage source was inserted in the middle of the plane ahving 1V at 0 degrees. An RLC load was connected to one of the wires, then the whole structure was selected in order to distribute this load to the whole system. A transmission line was connected to each wire originating from the source having characteristic impedance of 50 ohms. Finally, the ground parameter was selected as free space. Far field patterns, and frequency sweeps between 0.03 MHz and 35 MHz were obtained for the three different lengths of the antennae in order to properly compare them.
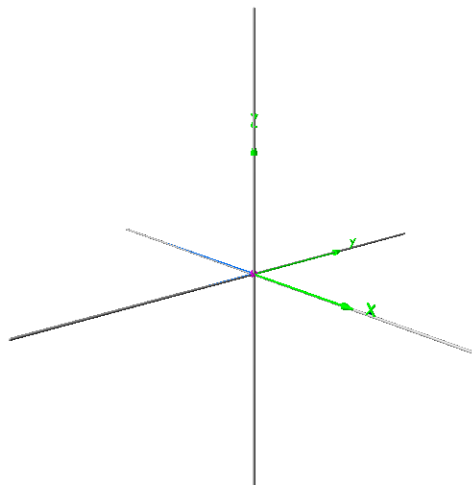
Figure 3.8: 3D view of the 7.5 m tripole. Source: 4nec2.

Below figures 3.9 and 3.10 show the far field pattern for the 7.5 m tripole antenna, exhibiting a maximum gain between -13 and -10 dBi.
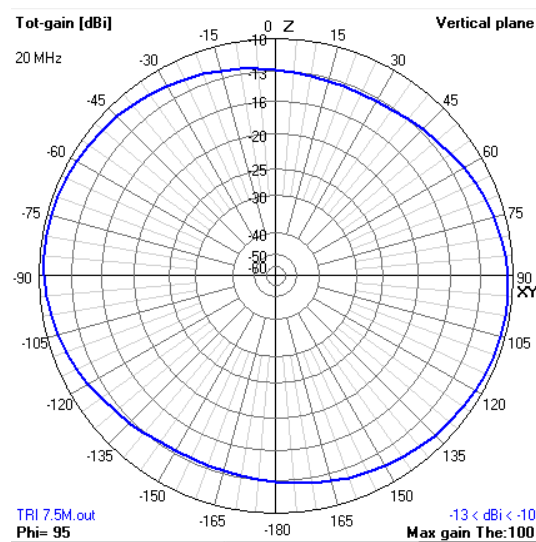
Figure 3.9: Pattern for 7.5 m tripole. Source: 4nec2.
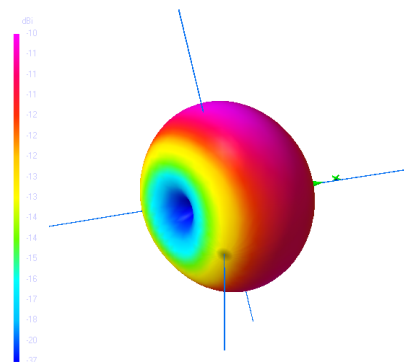
Figure 3.10: 3D Pattern for 7.5 m tripole. Source: 4nec2.

Figures 3.11 to 3.13 show the frequency sweep for the 5 m, 7.5 m, and 15 m tripoles respectively. For the 5 m tripole, the minimum reflection coefficient and standing wave ratios correspond to a frequency of 27 MHz, which is a bit far from the chosen 20 MHz detection frequency. The frequency sweep for the 7.5 m tripole show a better result where a more pronounced minimum is seen for the reflection coefficient around 18 MHZ, also corresponding to the least value of the SWR. As for the 15 m tripole, two minima are seen around 8 MHz and 31 MHz. Although the 15 m tripole has higher gains (-11 <dBi< -7.6) it also shows higher impdence mismatches. As such, the 7.5 m antenna is the best choice for this specific study.
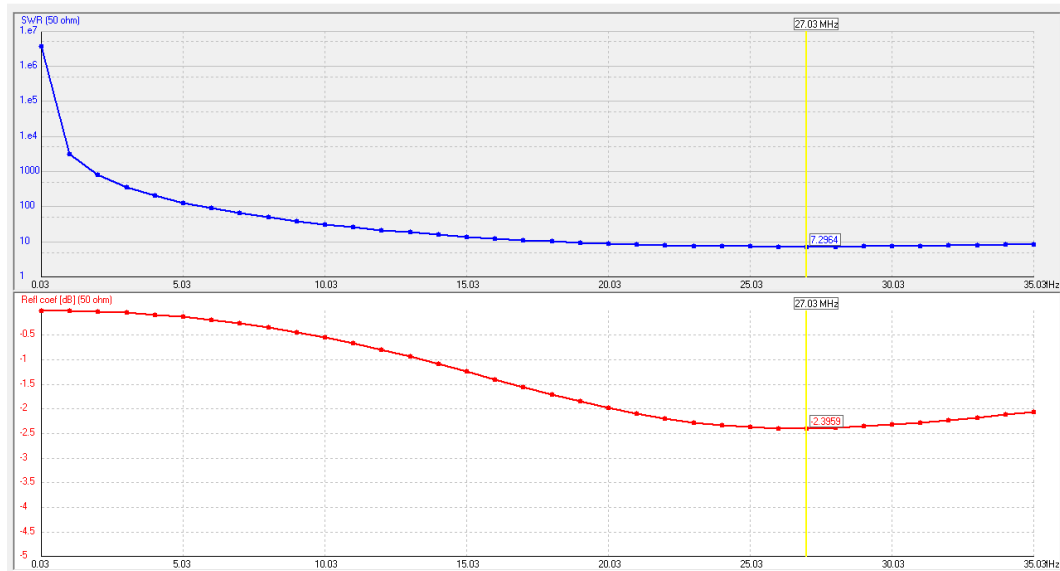
Figure 3.11: Frequency sweep for the 5 m tripole. Source: 4nec2.
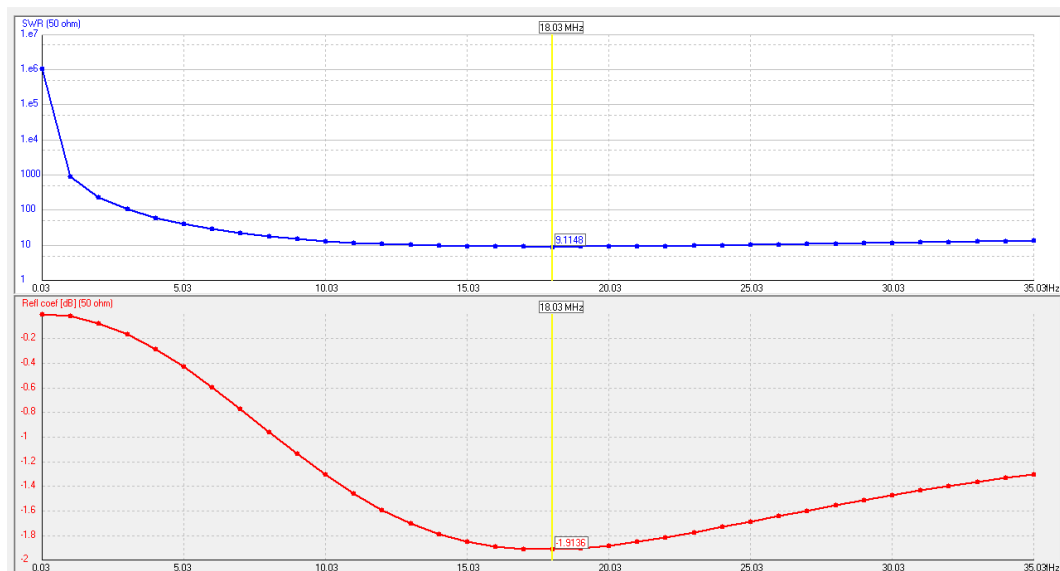
Figure 3.12: Frequency sweep for the 7.5 m tripole. Source: 4nec2.
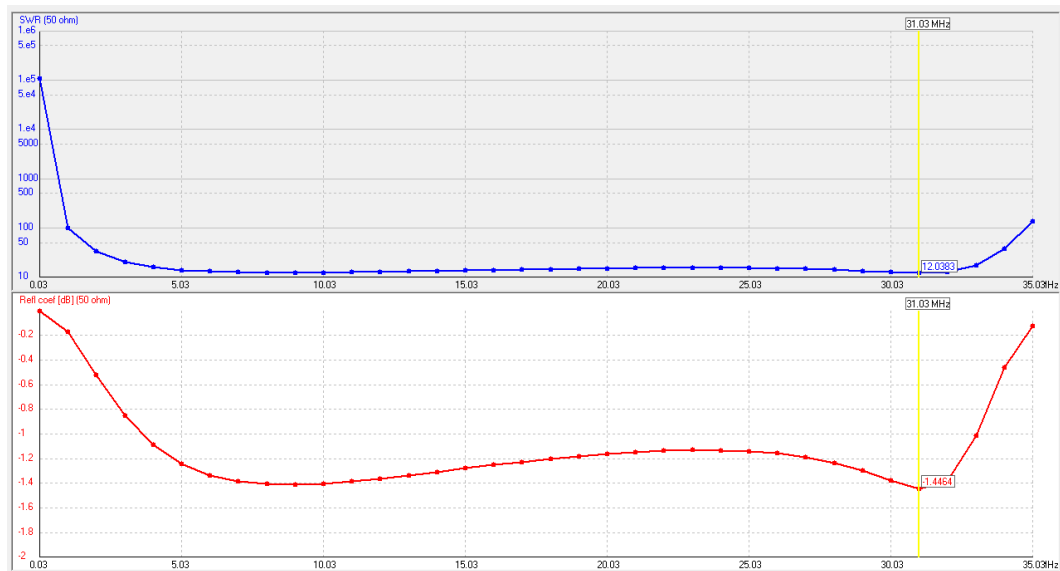
Figure 3.13: Frequency sweep for the 15 m tripole. Source: 4nec2.

3.7   Array Calculation

Using equation 3.14 from the Antenna Design section, several scenarios where calculated in order to determine the ideal amount of antennae needed for the required observations. A trade-off will be made between least amount of time and least number of antennae needed (lowest budget) while still having a reasonable outcome. The minimum number of CubeSats chosen is 9, knowing the fewer CubeSats will yield in inefficient survey times. The maximum number of CubeSats was chosen as per OLFAR mission (50 CubeSats). Two different numbers were then studied, first by slightly increasing the minimum number of CubeSats, to see the corresponding survey times. Second, the maximum number was cut in half in order to have a complete overview of these survey times.

The below calculations are based on a maximum baseline of 100 km, a resolution of $1'$, bandwidth of 27 MHz, varying number of dipoles from 27 to 150 (3 dipoles on each CubeSat), and for varying frequencies from 5 MHz to 30 MHz.

CubeSats	Dipoles	Survey Time (in days) at the below frequencies:			
		5 MHz	10 MHz	20 MHz	30 MHz
9	27	28.97	36.7	46	53
13	39	13.88	17.58	22.25	25.54
25	75	3.75	4.75	6	6.9
50	150	0.93	1.2	1.5	1.72

Table 3.3: Array analysis
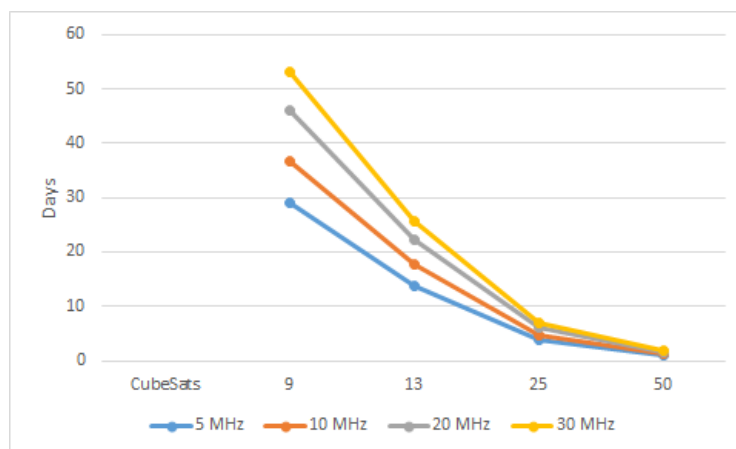
Figure 3.14: Range of survey times for different numbers of Cubesats

The results show that for a 9 CubeSat array, the survey time is the longest ranging from 4 to approximately 8 weeks in order to detect the required range. On the other hand, the array of 50 CubeSats (based on OLFAR number of CubeSats), shows a large difference in survey time needed (between 1 and 2 days) for the same range of frequencies. This huge difference comes at the cost of a large monetary budget. As the number of CubeSats are decreased, the survey times increase exponentially as seen in the plot of figure 3.14. Obviously having 50 CubeSats would be the ideal scenario, but a good compromise would be to use a 13 CubeSats array as it significantly differs from the 9 CubeSats by cutting the survey time to approximately half, while still respecting a reasonable budget for the project.

3.8   Conclusion

Tripole antennas with 7.5 m length will be used, mounted on CubeSats either orthogonal to each face of the cube or on the edge of the body to reduce the coupling between the antennae. Ideally multiple satellites will be used in order to increase the collecting area as much as possible. As per the previous calculations and analysis, 13 CubeSats will be used for this study, as they represent an acceptable trade-off between survey time and monetary budget. Obviously increasing the number of cubesats (up to 50 CubeSats in OLFAR's case) will improve the detections, but that will be at the cost of an increase in the budget. For the dark ages, the aim is to reach 5 mK error on the brightness temperature estimate at 20 MHz, within few month of the mission, allowing for the detection of the 21 cm line at SNR =10. The 5 mK error is reached by having > 60 dB pass-band calibration. Foreground substraction requires observation of the full band with a spectral resolution of 1 MHz.

Finally it should be noted that this discussion focuses on the main payload antenna needed to receive the 21 cm line. Other types of antennae are needed for inter-satellite communication and downlink to Earth, these will be further discussed in the next chapter within the whole architecture of the mission.

Chapter 4

THE NANO CUBESATS

Around 1000 Nano Cubesats have been launched since its inception around the year 2000. Initially developed as a project for graduate students, in order for them to have a better grasp on the design and concepts of satellites, it quickly showed its potential for scientific research and recently in the commercial world. Encorporating off the shelf material, building a Nano CubeSat is both cheap and fast, enabling several instituations and countries to utilize them for a wide range of applications (communications, weather monitoring, scientifical research...). One of the disatvantages of CubeSats is their short lifetime, mainly due to their low Earth Orbits, which is around 400 km. This low orbit will result in a fast decay and reentry, typically lasting for 2 years for a 400 km circular orbit. Other reasons for their short lifetime are due to poor quality standards that might be employed when building them. Despite all of that, they remain of great interest, considering that the pros outweight the cons, and with time, technology is improving the quality of manufacturing, assembly and validation of these satellites, making them more and more reliable.

4.1 CubeSat Description

CubeSats are small satellites whose basic unit form is a 10 cm edge cube, known as 1U (figure 4.1). CubeSat units can be assembled to form bigger entities, like 3U, 6U and so on. They must follow standards defined by the CubeSat design specification, which includes compliance with flight safety guidelines. Most of the subsystems used to assemble a CubeSat are commercial off-the-shelf components (COTS), and that is to ensure a low cost project. This means that large development teams are no longer needed, helping to reduce the costs even more. Budgets for CubeSats range between a few thousands to a few million US dollars, with development time spaning between a year and a couple of years.

A description of one satellite will be given in the following assuming that it is the same for the rest of the swarm. For this project 6U CubeSats will be used (with maximum allowed dimensions of: D:16.3 cm, W:14 cm, L:47 cm).

Figure 4.1: 1U CubeSat Platform. Source: isispace.nl.

4.2 CubeSat Architecture

Each CubeSat has a main payload, which is the element measuring or detecting the main science question of the mission. In this case, the main payload is the tripole antenna (along with it's subsystems: LNA and receiver) for the redshifted 21 cm line measurements. Other secondary payloads can be present as well, for this project the low frequency interferometer and spectrometer will fit in that category. For the attitude determination and control system (ADCS), a bias momentum wheel and eight attitude control thrusters are used. This ADCS should result in a pointing accuracy better than $1°$, an attitude stability better than $0.1°/s$, and attitude measurement better than $0.01°$. In addition to these components, the CubeSat should include a data concentrator (DCU), an onboard computer (OBC), a tranceiver (TRX) (in this case two tranceivers are needed, one for the inter-satellite link (ISL) and another for Earth Downlink (ED)), an electric power supply and solar panels. In addition inter-stage units, located in the space between two stacks of electronics, can serve for antennae fixing, and as an interface with the ground support equipment. Break-out boards are used to provide bus continuity between different electronic layers. Figure 4.2 shows the architecture used for the CubeSats, and figure 4.3 shows an example of the components used for the Hera 6U CubeSat.
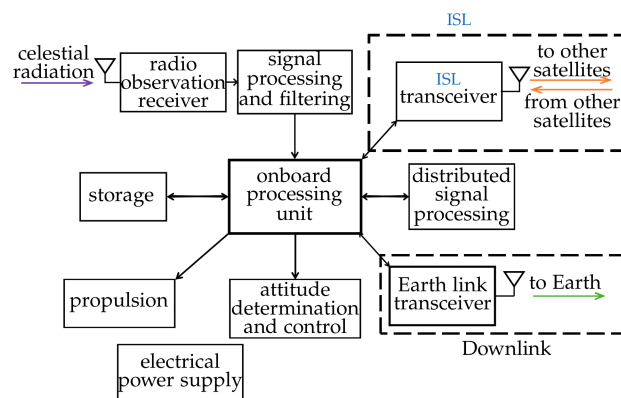
Figure 4.2: Architecture of a nanosatellite for radio astronomy. Source: Alexandru, 2015.

As can be seen from the figure above, the satellite should be able to perform a limited amount of tasks, in order to minimize the overall complexity of the system. (**6**)
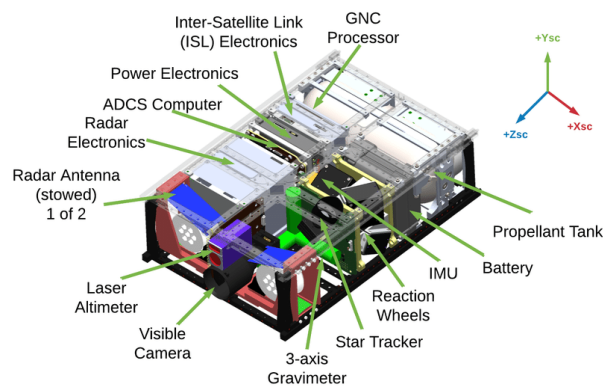
Figure 4.3: Hera CubeSat design with internal components shown. Source: International Astronautical Congress, 2018.

The previously mentioned components are arranged in a specific configuration, depending on the available space within each electronic stack, and on the particular constraints that each subsystem may have. An example of the structure configuration of a 2U is shown in the figure below. (**7**)
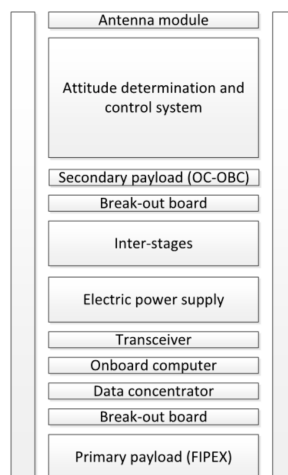
Figure 4.4: SE01 subsystem layout. Source: Cristobal Nieta-Peroy 2019.

The structure is mainly made out of aluminum alloys to conserve both weight and robustness. However, aluminum surfaces must be treated with a hard anodize coating to prevent cold welding and corrosion. In case there is a need for a conductive surface, the aluminum can be treated with chromate conversion coating.

Figure 4.5: Structural frame of a 6U CubeSat.

As for the bonding materials used, they range from epoxy (used for hard and lasting bonds), to room-temperature vulcanizing silicone (used as a filling and to fuse appendiges), to Kapton tape (used for labels, securing wires, holding components). These specific types are used because they do not suffer from outgassing, which is a frequent problem that affects most of bonding material.

Mass Budget

As per the CDS (CubeSat Design Specifications) the maximum mass allowed for a 6U CubeSat is 12 kg. Basing the mass study on the DSL mission which is quite similar to this project, the below table shows the approximate masses of the CubeSat's components,

Subsystem	Subsystem Mass (kg)
ADCS	1.08
Power	1.55
Propulsion	0.60
Structure	2.00
Thermal	1.00
Communications	0.50
Payloads	2.00
Data Handling	0.60
Total	**9.33**

Table 4.1: CubeSat Mass Budget

As such, the total mass of the CubeSat is below the maximum allowed mass of 12 kg, with a 2.67 kg margin for error.

4.3 Electronics & Connectivity

As per the PC/104 specification code followed in the CubeSat indusrty, all electronic boards must measure 90 x 96 mm^2, and the electric bus must allocate four rows with 26 contacs of standard 2.54 mm spacing through-hole (THT) headers. For the printed circuit boards (PCBs) the standard process for production can be adopted. Using color-coded wires, and labeling both ends is essential considering the huge amount of wires that is usually needed; moreover, proper simplified mapping of the wires and reducing their numbers should always be considered to reduce the overall complexity of the CubeSat.

Power Budget

The power supply collects, stores, and ditributes electricity to the rest of the subsystems in the CubeSat. An analysis of the power budget is crucial for the feasability of the mission and for the components sizing in the power supply chain. This power budget is also based on the DSL mission.

Subsystem	Subsystem Max Power (W)
ADCS	2.30
Power	0.00
Propulsion	2.00
Structure	0.00
Thermal	1.00
Communications	6.00
Payloads	4.00
Data Handling	3.00
Total	**18.30**

Table 4.2: CubeSat Power Budget

To compare, each of OLFAR's CubeSats will have a predicted maximum power consumption of 30 W. The installed solar panels should be able to collect these 19 W with an additional 20% of this total for emergencies to ensure a smooth operation of the CubeSat (a total of around 23 W). It should be noted that there is serious battery drainage when the CubeSats are collecting data, treating it and sending it, as such power management is necessary for a sustainable mission. Power managment strategies could entail a low power mode to recover the battery level for safe operations after every complete orbit of running the science task. A 340 x 180

x 1.6 mm solar panel that can be installed on any of the two largest sides of the 6U CubeSat can generate up to 19.4 W, thus two of these panels should provide more than enough power for the whole system (the additional power can be stored for emergency usage). Obviously the energy collection of the solar panels is dependant on the illumination; the more the panels have direct normal illumination from the sun, the more energy will be collected. Lithium-polymer batteries are used due to their small sizes and high energy densities.

4.4   Telecommunications

This project's swarm of CubeSats has three main functions regarding its role as a space-based interferometric array for radio asstronomy:

- · Observation of the redshifted 21 cm line
- · Distributed signal processing of the acquired signals
- · Cooperative downlink to Earth of the processed data
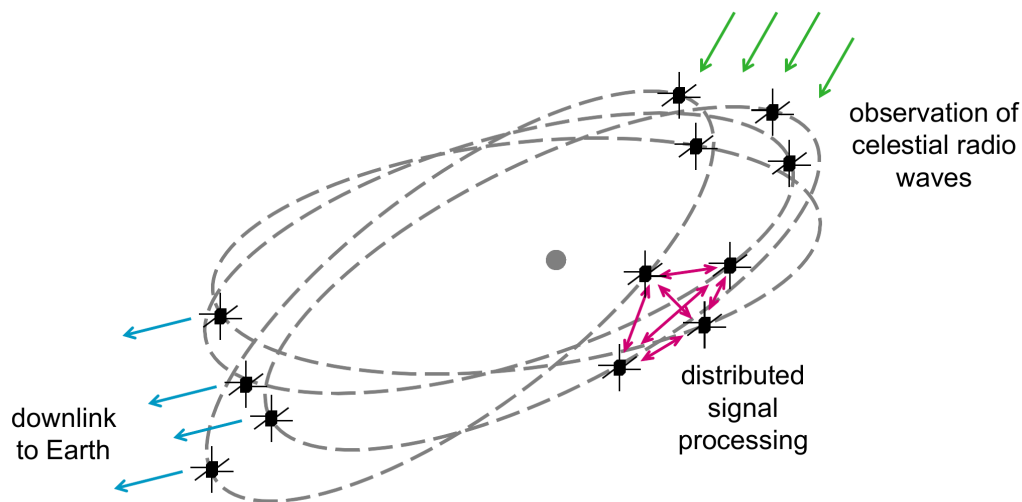
Figure 4.6: Different functions of the CubeSats sawrm. Source: Teodoro 2012

Each CubeSat in the swarm should be able to perform all of these tasks, meaning that each element is responsible for the redshifted 21 cm observations, sharing the received data with all other satellites, processing a certain frequency sub-band and downlink the processed data to Earth. A selection of 1000 narrow bands (1 KHz) within the 1-30 MHz range are used for interferometry. Figure 4.7 shows the functional components related to these tasks in each CubeSat. (**8**)
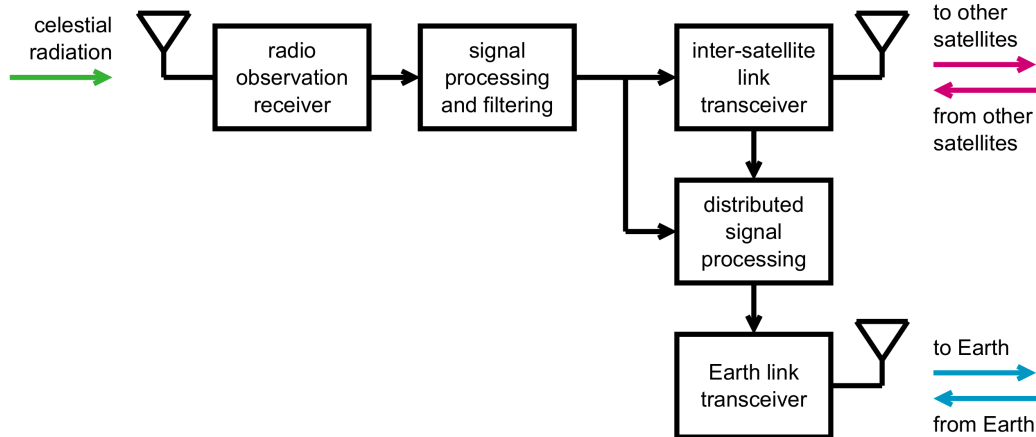
Figure 4.7: Functional components in each CubeSat. Source: Teodoro 2012

Inter Satellite Link

Sharing the data between the CubeSats will be done using RF links. Three main components are needed in order to perform this link: A data distribution strategy, baseband signal processing and an antenna system. For the data distribution, an adaptive clustering topology is proposed, in which each CubeSat can take one of two roles:

· Observation satellite, or slave, which performs the radio observations and shares its data by communicating with its cluster head.

· Cluster head, or master, which collects the information from the slave CubeSat and distributes it among the other cluster heads.

This topology ensures a reduction in the needed resources, mainly bandwidth and power, compared to a full-mesh peer-to-peer topology.

The signal processing in each CubeSat, generates data that determines the minimum required throughput of the ISL. It includes RFI mitigation techniques and filtering, resulting in a maximum data rate of 6 Mbit/s.

Six patch antennas ($9cm^2$ area each) are distributed on each face of the CubeSats as shown in figure below. These antennae are ideal for this task as they achieve the needed requirements and are practical to implement on the CubeSats. The proposed frequency band is 2.45 GHz, since it provides a suitable balance between antenna size, beamwidth and gain.

Below table shows the link budget for the ISL system,
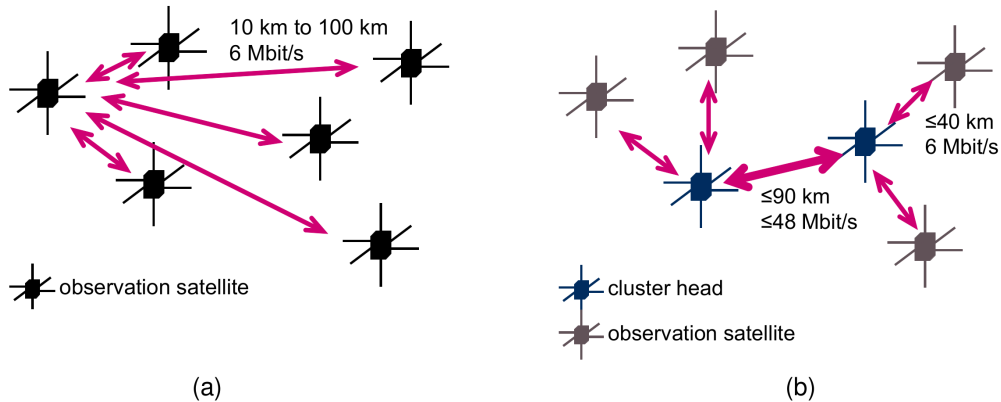
Figure 4.8: (a) Data distribution requirements and (b) their translation on the proposed clustering scheme. Source: Teodoro 2012
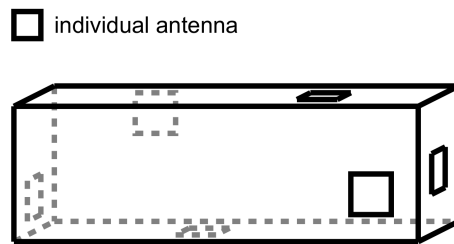
Figure 4.9: Proposed antenna configuration. Source: Teodoro 2012

Parameter		Value
Carrier frequency	f_c	2.45 GHz
Bandwidth	B	33 MHz
Link distance	r	90 km
Transmitter power	P_T	4 W
Transmitter losses	L_T	1 dB
Friis free-space loss	L_P	139.3 dB
Link margin	LM	2 dB
Receiver losses	L_R	1 dB
Signal-to-noise ratio	SNR	4.9 dB
Receiver noise figure	NF	4.6 dB
Noise floor	N	-107.1 dBm
Antenna system gain	G_T, G_R	≈ 5 dBi

Table 4.3: ISL Link Budget

Earth Downlink

Communication between the swarm and Earth can take two forms, either centralized or distributed. Figure 4.10 below shows a more accurate description of these

schemes. For this project a distributed scheme will be adopted, to increase redundancy of the overall system and in order not to completely rely on just one satellite for relaying all the data.
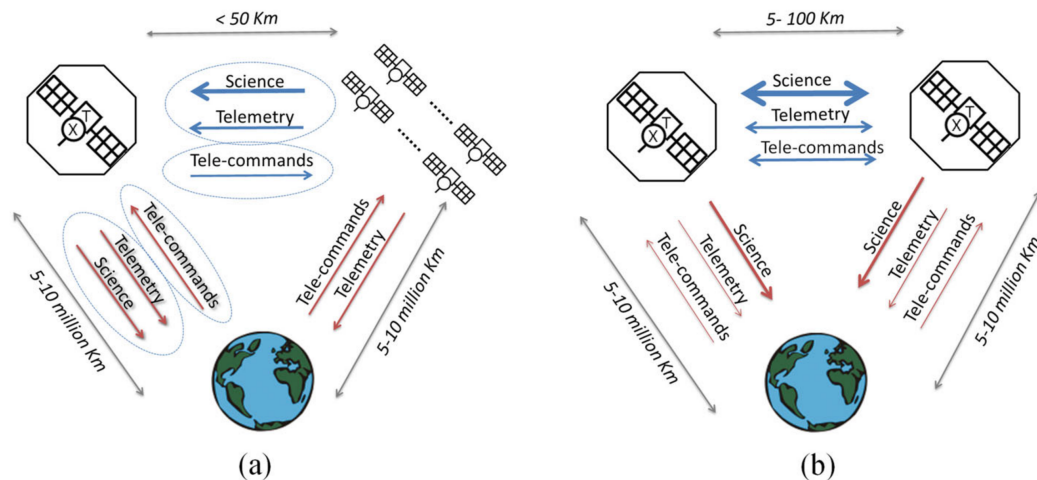
Figure 4.10: Communication architectures: An illustration of a (a) Centralized communication architecture and (b) single pairwise-link of a Distributed communication architecture for a space-based radio interferometric array. The Inter-satellite link is indicated in blue and the Earth-downlink by red. Telemetry and Tele-commands are exchanged between the satellites and with Earth in both scenarios. In case of the centralized scenario, we assume that the mothership is in the center of the array with a maximum mothership-node distance of 50km. Source: Teodoro 2012

Good communication links between the swarm and the ground station on Earth are essential for the downlink process. The parameters of a typical CubeSat to base station link are summarized in table 4.4. (**9**)(**10**)

4.5 Verification & Validation

During assembly of the CubeSats, they undertake a series of testing in order to make sure that they can witstand the harsh environment of space where they will be finally released. By doing so, adjustments can be made to the CubeSats, and the overall system can be evaluated whether it is still within the budget or not. So this is a crucial step when finalizing any CubeSat project. This procedure follows a set of approved upon guidelines such as the QB50 requirements. The 13 CubeSats of this mission should undertake these test. Ideally a prototype is made on which all test are conducted, after which the remaining CubeSats are assembled and tested. This will greatly improve assembly procedures and overall time.

Parameter		Value
Carrier frequency	f_c	2.45 GHz
Transmission power	P_{TX}	4 W
Transmitter/receiver losses	L_{TX}, L_{RX}	1 dB
Transmitting antenna gain	G_{TX}	5 dBi
Path loss	PL	212 dB
Link margin	LM	5 dB
Receiving antenna gain	G_{RX}	60 dBi
System noise temperature	T_{sys}	140 K
Antenna noise temperature	T_{ant}	40 K
Data rate	D_{down}	900 kbps
Coded data rate	$D_{downcoded}$	1200 kbps
Bandwidth	BW	630 kHz
Noise floor	N	-118.1 dBm
Signal-to-noise ration	SNR	0 dB

Table 4.4: Link Budget for worst-case scenario of swarm to Earth communication

Functional Tests

The functional test checks the CubeSats softwares, and if they are properly doing their allocated tasks. It mainly focuses on the functions that ensures the CubeSat's survival, like communications, power distribution and fault management. Certain functions, such as attitude control and orbit positionning cannot be tested in Earth environment; instead, a hardware-in-the-loop (HIL) simulation platform is used to emulate the space conditions. HIL is a type of real-time simulation used to test complex embedded systems (such as electronic boards) without the need of putting the product under the real physical conditions. It tricks the controller into thinking it is in the final assembled product, and thousands of possible scenarios can be easily tested without the cost and time associated with actual physical test. This test is frequently done, in order to properly assess the evolution of the CubeSat.

Mechanical Tests

Using an electrodynamic shaker, multiple mechanical tests can be performed. Figure 4.11, shows an example of a CubeSat in a 3U fixture mounted on a shaker through a head adaptor. Some of these mechanical tests include, a resonance test, a sine vibration test, a quasi-static acceleration test, shock tests and random vibration tests.
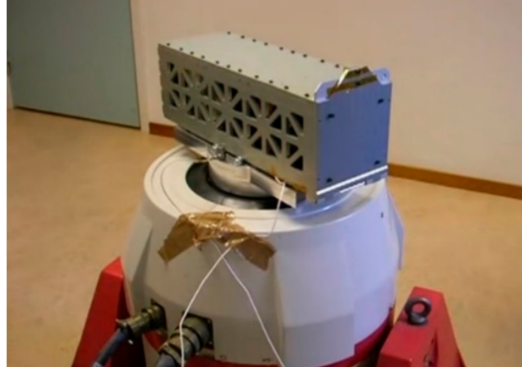
Figure 4.11: SE01 in a 3U fixture on the electric shaker facility. Source: Cristobal Nieta-Peroy 2019

Thermal-Vacuum Tests

These tests, simulate the extreme conditions of temperature and vaccum in the space environment to which the CubeSats are exposed to, in order to evaluate their behavior. They are time consuming and require constant monitoring during temperature transitions. The thermal-vaccum bake-out test (TVBO) checks for abnormal behaviors in the CubeSat when exposed to high temperature and very low pressure (mainly focuses on detecting outgassing materials in the CubeSat). The CubeSat cannot lose more than 1% of its mass after the end of the test, in order to pass the test. The thermal-vaccum cycling (TVC) test, checks for the CubeSat's behavior under extreme temperature changes in vaccum.
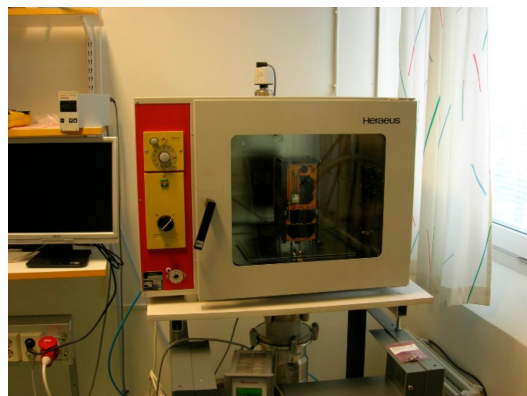
Figure 4.12: SE01 in the bake-out chamber. Source: Cristobal Nieta-Peroy 2019

4.6 Packing & Transportation

After finishing all the required tests, the CubeSats need to be properly packaged and delivered to the launch service provider. Packing the CubeSats can be done using a

vacuumed sealable antistatic bag, although leaving some air inside the bag could act as a cushion and help protect the CubeSat against hard impacts. Methacrylate covers are used to protect the solar panels which are easily scratched. Finally a schock-absorbent suitcase is used to safely transport the CubeSats. Some requirements need to be met during the transportation phase, such as an export license issued by the customs offfice. Delivering the CubeSats in person might be the safest way for the package to reach its final destination, as typical delivery services do not take responsibilty for any inflicted damage, and do not offer any reasonable insurance for such packages. The 13 CubeSats will be mounted on a specifically designed rocket that will launch them from the space station and release them into their final lunar orbit once they reach it. This rocket can be considered as a taxi, it should be able to return to its base station on Earth and be ready for other deliveries (this should be achievable in the near future, considering SpaceX's recent breakthroughs in developing reusable space shuttles).

Chapter 5

THE MISSION

A lot of space missions have been recently planned and are underway for the exploration of the redshifted 21 cm line. OLFAR and DSL are among those that will be targeting the farside of the moon to acheive these observations. This work builds on such missions while trying to extract the most convenient methods needed in order to study the Dark Ages specifically at the lowest cost possible.

This chapter is composed of two sections; the first part will focus on the mission's outline, from the CubeSats design and assembly to launch, while the second part will focus on the orbits determination and simulation.

5.1 Mission Outline

The project will be dissected into several phases, each focusing on a certain aspect of the mission. A typical mission life cycle is shown in figure 5.1 where the ECSS (European Cooperation for Space Standardization) defined milestones are given alongside additional NASA defined milestones.

Activity	Phases						
	Phase 0	Phase A	Phase B	Phase C	Phase D	Phase E	Phase F
Mission/Function	MDR◆ MCR▽	PRR◆					
Requirements			SRR◆ MDR▽ SDR▽	◆PDR			
Definition				CDR◆			
Verification					QR◆ SAR▽ ▽FRR	✦Launch	
Production					AR & ORR◆		
Utilization	ECSS Defined Review ◆					FRR◆ LRR◆	◆CRR
Disposal	NASA Defined Review ▽						ELR◆ MCR◆ DR▽

MDR	Mission Definition Review	AR	Acceptance Review
MCR	Mission Concept Review	ORR	Operational Readiness Review
PRR	Preliminary Requirements Review	FRR	Flight Readiness Review
SRR	System Requirements Review	LRR	Launch Readiness Review
SDR	System Definition Review	CRR	Commissioning Result Review
PDR	Preliminary Design Review	ELR	End-of-Life Review
CDR	Critical Design Review	DR	Decommissioning Review
SAR	System Acceptance Review	MCR	Mission Close-out Review
QR	Qualification Review		

Figure 5.1: A typical space mission life cycle with ECSS and NASA defined milestones. Source: The International Handbook of Space Technology.

Pre-Design Phase

In this phase, a timeline is set for the whole project, usually dictated by the available budget, it is one of the most crucial parts of the mission. A two year timeline will be considered for this endaevour, considering that it's a small scale architecture, but also enough time should be allocated for the technologies needed to proceed with it.

Each of the phases is acheived with its specific review, that detremines whether it is possible to proceed to the next phase or not. This phase encompasses phases 0 and A from figure 5.1; (**11**)

Phase 0: Mission Analysis
In this phase, the main objective is the analysis of the mission in order to identify the planned goals.

End of phase review: Mission Definition review (MDR)

Phase A: Feasibility
Compilation of different solutions and system concepts and finalizing the mission characteristics and functional requirements.

End of phase review: Preliminary requirements review (PRR)

In this case, the goal is the detection of the redshifted 21 cm line from the Dark Ages, and the feasability is mainly dependant on the budget which also affects the timeline. In order to proceed with this goal, an interferometric array of tripole antennae will be used.

It is also advisable to start the CubeSats registration process and frequency allocation at this stage, as they usually take a while to finalize. These will cover the legal steps needed for any satellite, and might affect the final design, especially the frequency allocation. The CubeSat registration is handled by the ITU (International Telecommunication Union). In case the cubesat will operate with a commercial telecommunication frequency, the frequency allocation is handled by the ITU. However, most of CubeSats operate with radio amateur frequencies, because they are free of charge; The frequency allocation of these satellites are done with the IARU (International amateur radio union).

A ground station development should also start early as it is time consuming, and critical for the operation of the swarm.

Phase B: Preliminary Definition Phase
Two goals need to be acheive during this phase; first, preliminary definition of the

mission with selection of possible technical solutions for the system concept chosen in the PRR.

End of phase review: System requirements review (SRR)

The second part focuses on further detailing, selection and definition of methods, resources and products including estimation of effort and implementation planning.

End of phase review: Preliminary definition review (PDR)

This part relies on information provided in chapters 3 and 4 concerning the antenna and the CubeSats.

Phase C: Detailed Definition Phase

Detailed investigation of the selected solution supported by manufacturing and qualification of representative elements, confirmation of feasibility and fulfillment of requirements.

End of phase review: Critical design review (CDR)

This part will also focus on chapters 3 and 4 with even more details in order to properly proceed to the next phase.

Phase D: Production Phase

Manufacturing, assembly, integration and testing are done in this phase. Procurement of components, manufacturing of first models (qualification model) for qualification of the selected design, verification of manufacturing methods and procedures.

End of phase review: Qualification review (QR)

Second step is the manufacturing of flight models on the basis of qualification test results, verification of reliable manufacturing, proof of functional performance and operation, and release for transport to the launch pad.

End of phase review: Acceptance review (AR)

Here the production of the payloads, the subsystems and NanoCubsats starts. Quality assurance (QA) and proper documentation are essential from this point and forward. QA ensures that the work done is in conformity to the established standards and up to the stakeholders' expectations. Good documentation helps to keep track of the evolution of the project, and in case any mistakes were made, they can be easily traced. It should also be mentioned that special facilities are needed for the fabrication process. Such facilities should include a workshop that provides all the

necessary machines, tools and equipment needed and clean rooms with specific standards (FED_STD-209E, or ISO 14644-1) where some of the assembly and all testing take place.

Phase E: Operation Phase

First part in this phase is the launch and early operation phase, where the functional performance of the overall system is evaluated, and a rehearsal for the mission is performed.

End of phase review: Operational readiness review (ORR)

Second is the preparation and execution of the launch campaign, and the satellite is released for launch.

End of phase review: Flight readiness review (FRR)

Finally, the satellite and overall system are commissioned for operation. The Cube-Sats are packaged and delivered to the launch service provider as detailed in the previous chapter.

Phase F: Disposal Phase

This phase includes the conclusion of the end of life performance and system deactivation. (**12**)

5.2 Orbit Design (Using STK)

In this section, the space mission (the operational phase between phases E and F in the above) will be computed through STK software. Systems Tool Kit (STK) is a physics-based software that displays and analyzes space assets among other things in real or simulated time. This task will be divided into two simulations. The first is using the Astrogator propagator, where the spacecraft is launched from Earth and goes into a trans-lunar injection, where it's trajectory is set for an orbit around the moon. After reaching the space around the moon, a lunar orbit injection is performed where the satellites are set into their final fixed orbit around the farside of the moon. This is where the second simulation starts, consisting of a constellation of 13 satellites. Before getting into the simulations, the proper orbit for the swarm of CubeSats needs to be determined; this is done at the begining of the next section.

Earth to Moon

Choosing the perfect orbit is quite a challenge, as multiple candidates are available. These locations vary from the Sun-Earth L4 or L5, Sun-Earth L2 lagrangian points, Earth-Moon L2, and lunar orbit.

(a) Sun-Earth Lagrangian points   (b) Lunar orbit
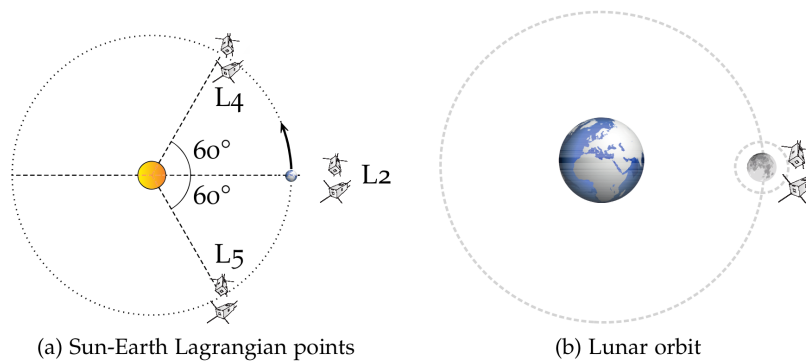
Figure 5.2: Possible deployment locations for the swarm of satellites. Source: Alexandru, 2015.

The lagrangian points have the advantage of being stable, and free from the man-made RFI. As such, not much propellant fuel is needed to maintain the CubeSats in orbit. On the other hand, their disatvantage is their remotness; being this far from Earth, makes it difficult to maintain radio connection with the swarm. A lot of energy will be needed to establish communications, no to mention more fuel is needed to reach the lagrangian points and release the swarm in their desired orbit. Thus, the lunar orbit will be considered for this project.

As previously stated, the absence of a thick atmosphere on the moon is of great importance as it provides somewhat uninterrupted reception of low frequency signals. Moreover, the farside is always shielded from electromagnetic interference generated from human activity on earth. Ideally, a stalletite in a lunarstationary orbit around the dark side of the moon should be a perfect candidate for the best detection of the redshifted 21 cm line. In a lunarstationary orbit, the satellite maintaines a fixed location relative to the moon, unlike a circular orbit where the satellite's rotation is in constant change with respect to the moon. However, achieving a lunarstationary orbit is not an easy task. For a satellite to be in a stationary position above the moon it has to be 88417 km away from its center (using Kepler's law for a selenostationary orbit),

$$a = \left(\frac{P^2 G M_{Moon}}{4\pi^2}\right)^{1/3} \tag{5.1}$$

Where P is the orbital period equals to 27.321 days, and G is the gravitaional constant.

Unfortunately, this distance is beyond the moon's Hill Sphere (radius at which the moon still maintains gravitational control over its satellites, $r = 52700$ km),

$$r \approx a_{Moon}(1 - e_{Moon})\sqrt[3]{\frac{M_{Moon}}{3M_{Earth}}} \tag{5.2}$$

Where $a_{Moon} = 348399$ km is the moon's semi-major axis around the Earth, and $e_{Moon} = 0.0549$ is the moon's orbital eccentricity. A more accurate result is achieved when taking the sun's gravitational effects into account, resulting in $r = 58050$ km, still way far from the desired distance to have a stationary orbit.

As such, a stationary orbit cannot be achieved around the moon due to Earth's gravitational pull. That being said, most of the orbits around the moon, even at low altitudes (Low Lunar Orbits), are unstable. That is mainly due to the gravitational anomalies present on the moon's surface, exhibited by mascons. These mass concentrations degrade orbits because of the non-unifrom gravitation fields that they create, affecting satellites that are passing over them.

However, there exists certain orbits were the satellites can be stable. Mainly four "frozen orbits" can be identified at 27°, 50°, 76°, and 86° inclination. The DARE mission that will be launched in the near future, works on another frozen orbit of inclination between $0 - 3°$ having an altitude of 50×125 km. The interesting part of this orbit is that it fixes a stable periapsis longitude (longitude at which the periapsis would occur if the body's orbit inclination were zero) of 180° which remains fixed over the farside of the moon. This is ideal for this specific scientific mission because it maximizes the observational time without the need for orbit maintenance maneuvers during the mission's lifetime. Figure 5.3 below shows the stability of the orbits at these specific altitudes.

During its 2 years of operation DARE will provide a total of 1150 prime science observation hours, much more than its predecesors. As such, this project's orbit design will build upon DARE's trajectory design, which results in a frozen circular orbit. (**13**)
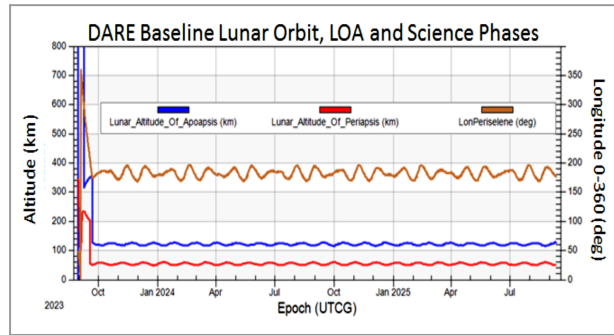
Figure 5.3: Timeline of LOA and science phases, The 2-year DARE lunar orbit with 50 x 125 km altitudes, inclination 1.72°, and longitude of periselene frozen near 180°. Source: Laura Plice 2017.

Figure 5.4, shows the DARE trajectory for all mission phases up until the early science phase, and Table 5.1 lists all the maneuvers needed to achieve the frozen orbit.
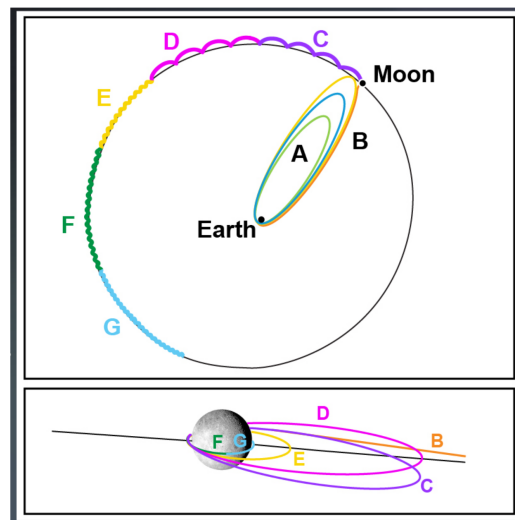
Figure 5.4: DARE trajectory showing phasing orbits (A), lunar transfer (B), lunar insertion 18 hr orbit (C), inclination trim from 5 or 20 deg to equatorial 0 - 3 deg (D), apoapsis lowering into 4 hr orbit (E), staging orbit (F), and frozen science orbit at 50 x 125 km (G). Source: Laura Plice 2017.

The transfer maneuvers needed to reach the final desired orbit require the management of three parameters: Alignment of the line of apsides, and altitudes of both apsides (aposelene and periselene). Hohmann transfer is used to maneuver between orbits at the right times and altitudes. As can be seen from Table 5.1, several maneuvers are needed to acheive the required orbit after the phasing loop transfer to the moon. Ranging from the calibration of propulsion subsystems, to plane

Mnvr #	Approx. Days from Launch	Days from Previous Maneuver	Maneuver Type	Nominal Magnitude or Allocation (m/s)	Description
--	<0.1	N/A	N/A	N/A	LV Phasing Orbit Injection & Separation
1	3	N/A	Engineering	10	AM1 Calibration of propulsion subsystem
2	6	3	Deterministic	31	PM1 Apo raising & phasing*
3	9	3	Deterministic	<10	PAM (Plane change to compensate for launch window)
4	14	5	Deterministic	3	PM2 Apogee raising & phasing*
5	24	10	Deterministic	0	PM3 Apogee raising*
6	25	1	Statistical	<5	TCM1 Correction
7	27	2	Statistical	<5	TCM2 Correction
8	29	2	Deterministic	304	LOI1 capture into 18 hour orbit
9	32	3	Deterministic	14	LIM (Lunar Inclination Maneuver)
10	35	3	Deterministic	269	LOI2 lowers aposelene (4 hr. orbit)
11	38	3	Deterministic	227	LOI3 lowers aposelene
12	48	9	Deterministic	31	OLM1 Orbit Lowering Maneuver - Periselene
13	51	3	Deterministic	47	OLM2 Lower Aposelene
14	Variable	Variable	Deterministic	<7	RFI avoidance if needed
15	780	Variable	Deterministic	10	Deorbit
					*Varies with launch day

Table 5.1: DARE Trajectory Maneuvers. Source: Laura Plice 2017.

changes, several days are required to achieve these before finally starting the Lunar Orbit Insertions. Three LOIs are needed with one Lunar Inclination Maneuver in between LOI1 and LOI2 to reach the $0 - 3°$ inclination needed. Fianlly, after 48 days from launch, the Orbit Lowering Maneuver can start for Periselene and Aposelene respectively (OLM1 and OLM2). Figure 5.5 shows the Orbit Lowering Approach for different design cases during a one year survey.

After establishing the desired orbit, the swarm is released into a linear formation to establish multiple baselines. As the array is circling, the baseline vectors between the CubeSats evolve, forming concentric rings in the *uv* plane as seen in figure 5.6. By varying the distance between the CubeSats and using bandwidth synthesis, the gaps between the rings can be partially filled. (**14**)
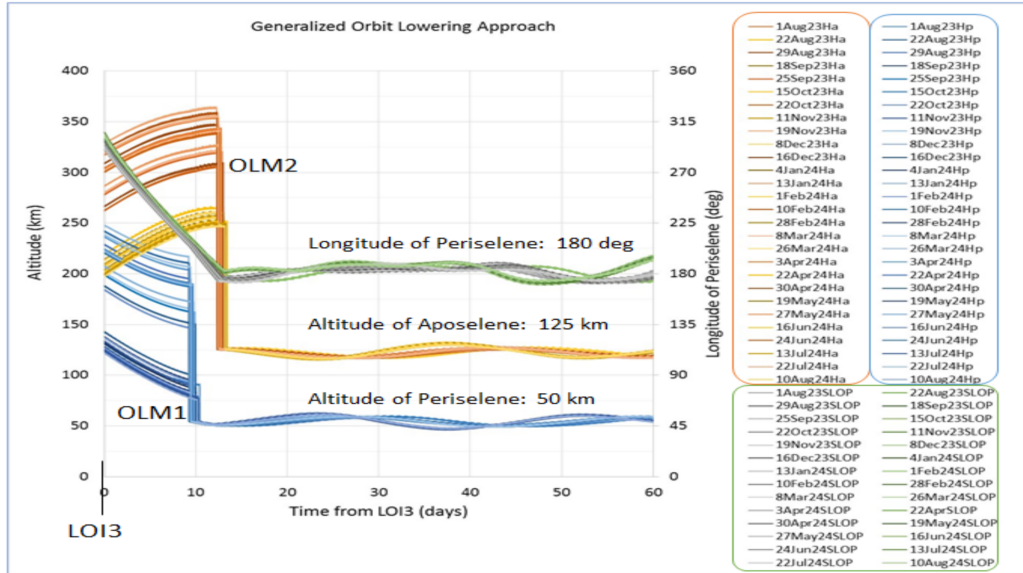
Figure 5.5: Orbit Lowering Approach Achieves the Frozen Condition by Timing of the Maneuvers. Source: Laura Plice 2017.
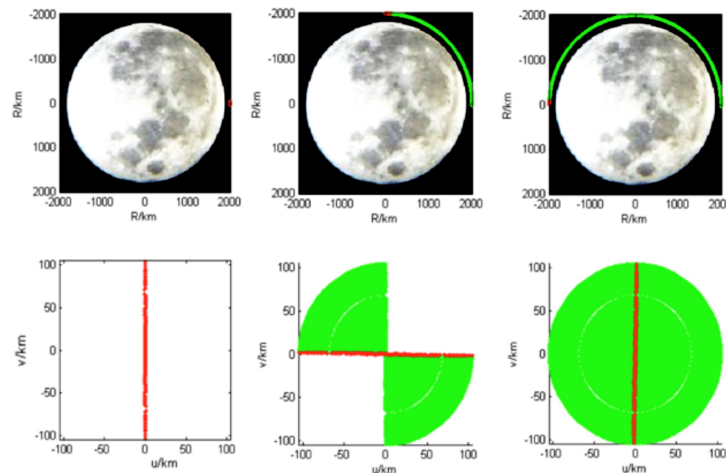
Figure 5.6: Evolution of the spatial aperture plane filling after one orbit of DSL (down) as it orbits the Moon (up). Source: Xuelei Chen.

The mentioned trajectory can be computed using STK, however, a lot of details are needed in order to properly model this trajectory (type of attitude control, maneuver type (impulsive or finite), plane changes and inclination maneuvers). Instead, a more general approach was adopted in order to show the trajectory from Earth to the Moon.

A Satellite with defined properties was selected from the objects list. In the basic orbit window that pops up, the Astrogator is chosen as the propagator. Then a new

segment is chosen (Earth to Moon), where the following parameters were adjusted: Lunar altitude of 125 km, and lunar inclination of 15 degrees. Lower inclinations did not result in a converged solution as more maneuvers are needed to properly reach this inclination. Based on these settings the Mission Control Sequence was initiated, the graphics were cleared and the initial time for animation was set.

Below are the resulting figures, showing different snapshots of the satellite's trajectory from initial launch in Florida till it reaches its orbit around the moon.

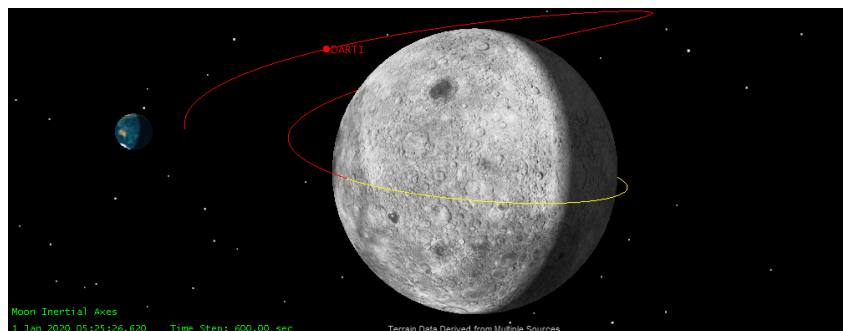Figure 5.7: Earth to moon launch - cut 1. Source: STK.

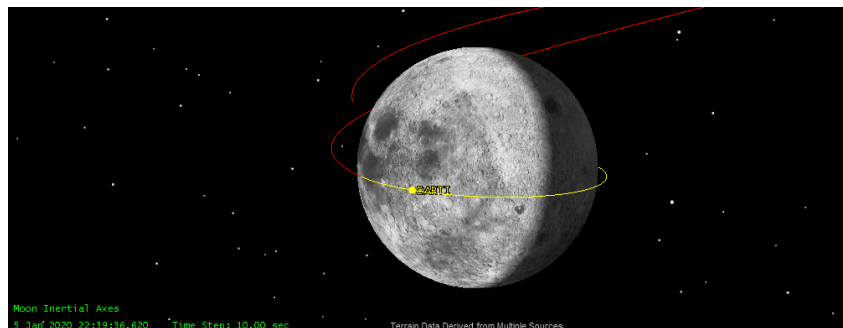Figure 5.8: Earth to moon launch - cut 2. Source: STK.

Figure 5.9: Earth to moon launch - cut 3. Source: STK.

Satellites Constellation

When the spacecraft reaches its frozen orbit, the satellites are released into their line formation. Ideally the formation should follow the one adopted in the DSL mission, where the baseline between satellites varies from 100 m to 100 km. A reconfiguration strategy for balanced fuel consumption for all satellites is needed, shown in figure 5.10, where the first satellite stops, until there is shrinkage in the baselines, after a certain time the last satellite is kept stationary, after which the rest of the swarm will expand from each other, so on and so forth (noting that the minimum and maximum baseline distances are the ones previously mentioned).
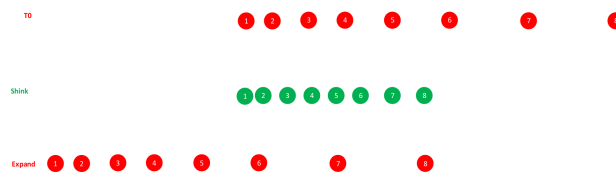

Figure 5.10: Formation reconfiguration strategy. Source: Xuelei Chen 2019.

In STK, after selecting the moon as the main body of reference, a satellite is inserted with the following orbit wizard parameters: Semimajor axis = 1825.9 km, Eccentricity = 0.0205, Inclination = 1.5 deg, Argument of Perigee = 180 deg, and RAAN = 330 deg (values selected for best case senario from Laura Plice paper).

After doing so a receiver is inserted for the satellite, having for type the multiple beam receiver. Each of the three beams is configured as the previously designed antenna in chapter three. The next step was to creat the constellation; using the walker tool, the number of satellites was selected as 13 in 1 plane, so that they will be in a linear formation. The ideal case was to select a custom type for the constellation, unfortunatly, this version of STK does not provide this option (only Delta, and modified delta formation are available). In the selected Delta formation, the satellites are equally spaced, which is not the case for this mission (spacing will be around 840 km between each satellite, while the maximum allowed spacing is 100 km).

As can be noted from figure 5.11, the orbit clearly shows the aposelene on the farside of the moon and the periselene on the nearside of the moon, which is the desired result. This stable orbit will provide each satellite one hour on the dark side of the moon and 56 mins on the other side for each revolution.
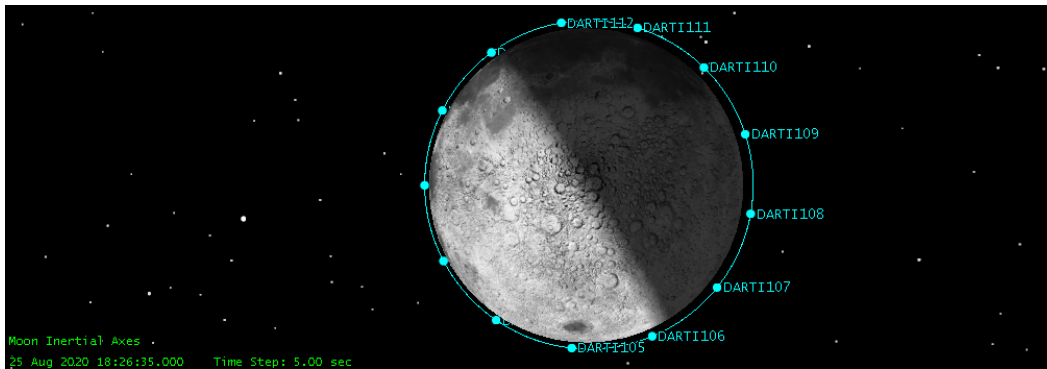
Figure 5.11: Satellite constellation top view. Source: STK.
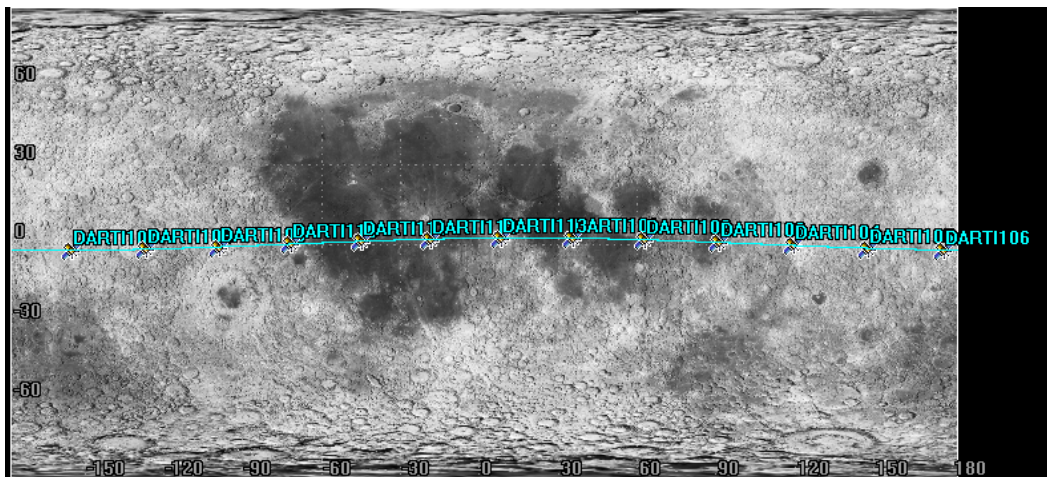
Figure 5.12: Satellite constellation planar view. Source: STK.

During the time the swarm is on the dark side, the antennae are picking up the redshifted 21 cm signal, treating it and storing it. When the swarm reaches the other side where it has a line of sight to Earth, it will initiate the downlink process to send the collected data back to the established ground stations on Earth.

A coverage report is generated for all of the satellites receivers. It shows a coverage of approx 5700 s (around 95 mins) for each receiver, and a mean duration of 5276 s (88 mins) for all the receivers. This result shows that the satellite has enough time during its one hour orbit around the dark side of the moon to collect the needed data. When comparing to a nine satellites array, its coverage is approx 2776 s (around 46 mins) for each receiver, and its mean duration is 5910 s (98 mins) for all the receivers. So decreasing the number of CubeSats from 13 to 9 will cut in half the amount of coverage needed for each receiver. This is consistent with the results achieved in the Array calculation section of the Antenna chapter, where it was concluded that decreasing the number of CubeSats to nine will double the amount needed for the

survey.

A coverage graph is also produced showing gaps throughout a daily coverage time-line.

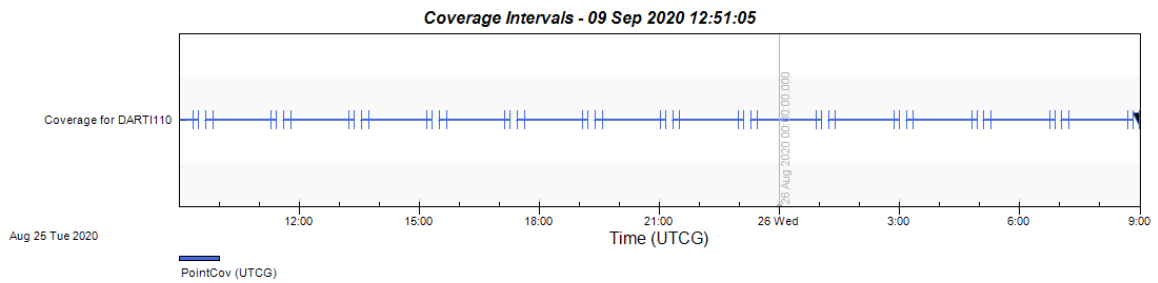

Figure 5.13: Coverage Intervals. Source: STK.

Page 1

                  09 Sep 2020 12:48:54
Coverage Intervals

Coverage for DARTI110

Access	Duration (sec)	Asset Full Name	Access Start (UTCG)	Access End (UTCG)
1	1735.472	DARTI109	25 Aug 2020 09:00:00.000	25 Aug 2020 09:28:55.472
2	1300.610	DARTI111	25 Aug 2020 09:00:00.000	25 Aug 2020 09:21:40.610
3	5920.764	DARTI111	25 Aug 2020 09:39:41.062	25 Aug 2020 11:18:21.827
4	5698.753	DARTI109	25 Aug 2020 09:50:37.931	25 Aug 2020 11:25:36.685
5	5920.760	DARTI111	25 Aug 2020 11:36:22.274	25 Aug 2020 13:15:03.034
6	5698.759	DARTI109	25 Aug 2020 11:47:19.139	25 Aug 2020 13:22:17.898
7	5920.759	DARTI111	25 Aug 2020 13:33:03.486	25 Aug 2020 15:11:44.245
8	5698.755	DARTI109	25 Aug 2020 13:44:00.355	25 Aug 2020 15:18:59.110
9	5920.763	DARTI111	25 Aug 2020 15:29:44.694	25 Aug 2020 17:08:25.457
10	5698.754	DARTI109	25 Aug 2020 15:40:41.563	25 Aug 2020 17:15:40.317
11	5920.761	DARTI111	25 Aug 2020 17:26:25.910	25 Aug 2020 19:05:06.671
12	5698.758	DARTI109	25 Aug 2020 17:37:22.777	25 Aug 2020 19:12:21.534
13	5920.764	DARTI111	25 Aug 2020 19:23:07.118	25 Aug 2020 21:01:47.883
14	5698.752	DARTI109	25 Aug 2020 19:34:03.989	25 Aug 2020 21:09:02.741
15	5920.759	DARTI111	25 Aug 2020 21:19:48.334	25 Aug 2020 22:58:29.093
16	5698.753	DARTI109	25 Aug 2020 21:30:45.202	25 Aug 2020 23:05:43.955
17	5920.762	DARTI111	25 Aug 2020 23:16:29.544	26 Aug 2020 00:55:10.306
18	5698.754	DARTI109	25 Aug 2020 23:27:26.412	26 Aug 2020 01:02:25.166
19	5920.764	DARTI111	26 Aug 2020 01:13:10.753	26 Aug 2020 02:51:51.516
20	5698.753	DARTI109	26 Aug 2020 01:24:07.624	26 Aug 2020 02:59:06.377
21	5920.765	DARTI111	26 Aug 2020 03:09:51.968	26 Aug 2020 04:48:32.732

```
Page 2
                Access       Access Start (UTCG)        Access End (UTCG)
      Duration (sec)   Asset Full Name
                ------   ----------------------   ----------------------
--  --------------   ---------------
                22   26 Aug 2020 03:20:48.838   26 Aug 2020 04:55:47.5
90         5698.752   DARTI109
                23   26 Aug 2020 05:06:33.180   26 Aug 2020 06:45:13.9
40         5920.759   DARTI111
                24   26 Aug 2020 05:17:30.044   26 Aug 2020 06:52:28.8
03         5698.759   DARTI109
                25   26 Aug 2020 07:03:14.392   26 Aug 2020 08:41:55.1
54         5920.762   DARTI111
                26   26 Aug 2020 07:14:11.261   26 Aug 2020 08:49:10.0
16         5698.755   DARTI109
                27   26 Aug 2020 08:59:55.599   26 Aug 2020 09:00:00.0
00            4.401   DARTI111

Global Statistics
-----------------
Min Duration    27   26 Aug 2020 08:59:55.599   26 Aug 2020 09:00:00.0
00            4.401   DARTI111
Max Duration    21   26 Aug 2020 03:09:51.968   26 Aug 2020 04:48:32.7
32         5920.765   DARTI111
Mean Duration
           5276.840
Total Duration
         142474.681
```

Chapter 6

CONCLUSION

To conclude, studying the Dark Ages is an exciting and necessary step into better understanding the formation and evolution of our universe. It is driven by the detection and study of the hyperfine splitting of the primordial hydrogen atom. The 21 cm line specific to this period in the expansion of the universe, reaches us with a doppler shift, meaning that its frequency is much lower than what it initially was. Having wavelengths between 10 meters and 1 kilometer, it requires proportional aperture sizes in order to detect it. When taking into account the RFI around the Earth's environment, it was concluded that the best location for such an observation is from the farside of the moon, which acts as a natural cover from unwanted EM waves. The received signal obviously needs to be treated to remove the foregrounds before being able to analyze it.

The large baseline that is required can be easily achieved using a swarm of CubeSats, carrying tripole antennae. This interferometric array will detect the redshifted 21 cm line while the swarm is on the dark side of the moon, then clean and communicate the data, and finally relay it back to Earth ground stations when the swarm reaches the other side of the moon. The antennae are three 7.5 meters copper wires orthogonal to each other.

Using the CubeSats as carriers of the array is an essential step for this mission as it reduces the system's overall complexity and cost. A set of thirteen 6U CubeSats should be enough to complete the desired task. The ideal orbit for the swarm is a circular frozen orbit 50 x 125 km around the moon. This special orbit with inclinations between 0 and 3 degrees allows for consistent scientificall observations with each revolution for a period of two years.

DARE, Farside, OLFAR, and DSL are among the space missions targeting the detection of this range of low frequncies (between 0.3 and 30 MHz or 30 and 200 MHz); they should be operational within a couple of years. This mission is a one of a kind study that builds on the best features of its predecessors, while taking into consideration the least monetary budget possible to achieve it. Hopefully these missions along with DARTI will bring back some groundbreaking discoveries, helping us better understand our lovely universe.

Below table shows a summary of the upcoming missions targeting similar studies as this reasearch paper (DARTI).

Name	Freq. range (MHz)	Baseline (km)	No. Sats	Antenna	Deployment location
DARE	40 - 120	0	1	Biconical dipoles	50 x 125 km Lunar frozen Orbit
DARIS	1 - 30	⩽100	6-8	5m tripole	Dyn. Solar Orbit
FIRST	0.5 - 50	⩽30	7	tripole	Sun-Earth L2
SURO	0.13	⩽30	8+	tripole	Sun-Earth L2
DSL	0.1 - 50	⩽100	8	7.5m tripole	300 km Lunar circular Orbit
NOIRE	0.001 - 100	⩽100	various	5m tripole	Lunar Orbit
RELIC	0.1 - 30	⩽100	33	5m dipole	Lunar Orbit
NCLE	0.08 - 80	0	1	5m tripole	Earth-Moon L2
OLFAR	0.1 - 30	100	⩾50	dipole or tripole	TBD
DARTI	0.3 - 30	⩽100	13	7.5m tripole	50 x 125 km Lunar frozen Orbit

Table 6.1: List of space-based low frequency radio observatories

BIBLIOGRAPHY

[1] S. Seager, D. D. Sasselov, and D. Scott. A New Calculation of the Recombination Epoch. ApJ, 523:L1–L5, September 1999.

[2] Jonathan R. Pritchard and Abraham Loeb. 21 cm cosmology in the 21st century. Jan 2012

[3] Steven R. Furlanetto, S. Peng Oh Cosmology at low frequencies: The 21 cm transition and the high-redshift universe Sep 2006

[4] Raj Thilak Rajan, Space-based aperture array for ultra-long wavelength radio astronomy Jun 2015

[5] Linjie Chen, Antenna design and implementation for the future space ultra-long wavelength radio telescope Feb 2018

[6] Alexandru Budianu, Echos from the past Jun 2015

[7] Cristobal Nieto-Peroy and M. Reza Emami, CubeSat Mission: from design to operation, Jun 2019

[8] Teodoro J. Willink, Antenna system design for OLFAR's inter-satellite link, Oct 2012

[9] A. Budianu, A. Meijerink, Swarm-to-Earth communication OLFAR, Nov 2014

[10] Nasir Saeed, CubeSat communications: Recent advances and future challenges, Apr 2020

[11] Malcom Macdonald, The international handbook of space technology, 2014

[12] Wilfried Ley, Handbook of space technology, 2009

[13] Laura Plice, DARE mission design, low RFI observations from a low altitude frozen lunar orbit, Jan 2017

[14] Xuelei Chen, Discovering the sky at the longest wavelengths with small satellite constellations, Jan 1019

INDEX